Ceramics International 52 (2026) 1013–1033

Contents lists available at ScienceDirect

Ceramics International

journal homepage: www.elsevier.com/locate/ceramint

Enhancing the CMAS resistance of YSZ thermal barrier coatings via hybrid suspension/solution precursor plasma spraying with gadolinium doping

Margherita Cescon [a], Stefania Morelli [a,b,f,*], Edoardo Rossi [c], Daniele Duranti [c], Wenjuan Cheng [c], Marco Sebastiani [c], Paola Palmero [d], Elisa Fiume [d], Bartolomeo Coppola [d], Alessandro Lanzi [e], Luca Lusvarghi [a,b,f], Giovanni Bolelli [a,b,f]

[a] Department of Engineering "Enzo Ferrari", Università di Modena e Reggio Emilia, Via Pietro Vivarelli 10/1, 41125, Modena, MO, Italy
[b] InterMech – MO.RE. Centro Interdipartimentale per la Ricerca Applicata e i Servizi nel Settore della Meccanica Avanzata e della Motoristica, Università di Modena e Reggio Emilia, Via Pietro Vivarelli 2, 41125, Modena, MO, Italy
[c] Department of Civil, Computer Science and Aeronautical Technologies Engineering, Università di Roma 3, Via Vito Volterra 62, 00146, Roma, Italy
[d] Politecnico di Torino, Department of Applied Science and Technology, INSTM R.U. Lince Laboratory, Corso Duca Degli Abruzzi, 24, Italy
[e] Lincotek Rubbiano S.p.A., Via Mistrali 7, 43046, Rubbiano di Solignano, PR, Italy
[f] Consorzio Interuniversitario Nazionale per la Scienza e Tecnologia dei Materiali (INSTM), Local Unit: Università di Modena e Reggio Emilia, Via Pietro Vivarelli 10/1, 41125, Modena, MO, Italy

ARTICLE INFO

Keywords:
Thermal barrier coatings
Rare earth-doped zirconia
Hybrid suspension/solution precursor plasma spraying
CMAS corrosion
Fracture toughness

ABSTRACT

Liquid feedstock plasma spraying is a promising method for producing thermal barrier coatings (TBCs) with a microporous structure, offering low thermal conductivity and good compliance to thermal stresses. However, the high porosity reduces their resistance to CMAS (calcium–magnesium–alumino–silicate) infiltration. This study explored a hybrid suspension/solution precursor plasma spraying (SPS/SPPS) technique to improve CMAS resistance and thermal cycling performance. A 25 wt% 8YSZ suspension in ethanol was doped by dissolving various concentrations (0.25 M, 0.50 M, and 0.75 M) of $Gd(NO_3)_3{\cdot}6H_2O$. Coatings were deposited on Hastelloy-X substrates with a NiCoCrAlY bond coat, both as single layers and as top layers over conventional porous or dense-vertically cracked (DVC) 8YSZ. Microstructural, phase, and micromechanical analyses, including pillar splitting tests, were performed. Gd-doping enhanced the CMAS resistance by forming a protective apatite phase, although its benefits plateaued beyond a certain concentration. This method offers a flexible, cost-effective route to advanced TBCs.

1. Introduction

Thermal Barrier Coatings (TBCs) are coatings designed to thermally insulate the metallic components of gas turbines, which are often exposed to gas flows at extremely high operating temperatures, even above 1400 °C [1,2]. These coatings play a crucial role in improving the reliability and lifespan of turbines by protecting the metal parts from heat-induced damage and from corrosion by calcium–magnesium-alumino-silicate (CMAS) molten deposits.

In dusty environments, solid oxide particles can be ingested into the turbine through the inlet air and, at high temperatures, they melt creating a glassy deposit which is one of the main reasons of coating failure [3–6]. The state-of-the-art material used as ceramic topcoat of TBCs is zirconia stabilized with 8 wt% of yttria (8YSZ). It possesses a very low thermal conductivity, which is 2.3 W m^{-1} K^{-1} at 1000 °C for a fully dense material [7], and high thermal expansion coefficient (CTE) of approximately 11 × 10^{-6} K^{-1} over the 293–1273 K range [8,9], helping to alleviate the stress caused by the expansion mismatch between the topcoat and the metal substrate. However, despite its numerous advantages, 8YSZ is prone to long-term phase change at temperatures above 1200 °C. Furthermore, under CMAS corrosion, a dissolution and re-precipitation mechanism occurs where CMAS dissolves 8YSZ along its grain boundaries, weakening the structural integrity of the coating. Additionally, yttria-depleted zirconia can re-precipitate, which transforms from the high-temperature tetragonal phase to the monoclinic phase during cooling. This phase transformation results in a significant volume change (4 vol%), which further increases the internal stresses within the coating and contributes to coating spallation [5,10–14].

* Corresponding author. Department of Engineering "Enzo Ferrari", Università di Modena e Reggio Emilia, Via Pietro Vivarelli 10/1, 41125 Modena, MO, Italy.
E-mail address: stefania.morelli@unimore.it (S. Morelli).

https://doi.org/10.1016/j.ceramint.2025.11.400
Received 18 September 2025; Received in revised form 19 November 2025; Accepted 26 November 2025
Available online 26 November 2025

The traditional method for applying TBCs in industrial gas turbines is the Atmospheric Plasma Spraying (APS) process [15–18]. However, the APS process has limitations, such as its inability to produce thin (less than 10 μm) and nanostructured coatings with microstructural features in the range of 1–100 nm, due to the restriction on using feedstock powders finer than 5–10 μm [19]. To address this issue, liquid feedstock plasma spray techniques such as Solution Precursor Plasma Spraying (SPPS) and Suspension Plasma Spraying (SPS) have been explored [20–24]. SPPS involves injecting into the plasma jet a solution containing a precursor of the coating material, while SPS uses nanometric or submicrometric particles dispersed in a suspension, which can be made with liquid media such as ethanol or water [20]. Both techniques involve a series of sequential stages, beginning with the fragmentation of the liquid stream into fine droplets upon injection into the thermal plasma plume. After this initial stage, the mechanisms diverge [25]. In the SPS process, fragmentation is followed by solvent vaporization, which results in the release of solid content in the form of individual particles or agglomerates. Some of these agglomerates may be disrupted during the process. The particles and agglomerates then melt and are deposited onto the substrate [26,27]. Key factors, such as the size of the initial solid particles, the agglomerates formed after solvent vaporization, and the size of the fragmented droplets, influence the deposition behavior and the final microstructure of the coating. In contrast, in the SPPS process, as the solvent vaporizes, the solute precipitates within the droplets. This is followed by a series of chemical reactions, such as gelation or pyrolysis, which lead to the formation of the coating material from the original precursor salts [28–30].

Through these techniques, it is possible to produce highly porous, columnar microstructures with very fine lamellae that offer reduced thermal conductivity, making them ideal for high-temperature applications [31,32]. However, the high porosity of these microstructures can lead to a severe corrosion by molten CMAS [21]. The molten CMAS deposits can easily penetrate the inter-columnar gaps and intra-columnar porosity, and attack the boundaries between fine yttria-stabilized zirconia (YSZ) grains. Due to the high porosity, this degradation mechanism is accelerated.

Extensive research was performed with conventional APS TBCs to explore alternative materials to 8YSZ that can offer enhanced resistance to CMAS. One of the most promising strategies involves the incorporation of rare earth elements into the coatings [14,33–36]. Previous research has shown that rare-earth zirconates ($RE_2Zr_2O_7$) coatings offer benefits in terms of resistance to CMAS corrosion [37,38]. Some rare-earth ions, such as Gd^{3+}, react with the glassy deposits, forming stable apatite crystals, that help prevent further infiltration of molten silicates into the coating layers [38–40]. This reaction is influenced by the optical basicity of the compounds involved [41,42]. Essentially, the greater the difference in optical basicity between CMAS and the rare earth oxide, the more reactive the materials are with one another, leading to the precipitation of protective phases.

It is thus interesting to explore the use of rare-earth doping also in liquid feedstock-plasma sprayed TBCs, trying to couple the specific advantages of the SPS/SPPS microstructures with the enhanced chemical resistance of doped zirconia. The incorporation of rare earth elements into zirconia coatings obtained by liquid feedstock plasma spraying can be done in two ways. With SPS, a pre-synthesized fine powder with the desired composition must be dispersed into the chosen liquid medium [43,44].With SPPS, suitable amounts of precursors of zirconia and rare-earth elements must be dissolved, and their reaction must then be achieved during spraying [45–47].

An interesting alternative is to employ a hybrid suspension + solution approach, whereby a suspension of 8YSZ is doped by dissolving precursor salts of rare-earth elements, seeking to achieve in-flight reaction to obtain a zirconia coating doped with both Y_2O_3 and the chosen rare-earth element. This approach can be considered an extension to and a refinement of the "hybrid" spraying of dry powders and liquid feedstock explored, for example, by Joshi and Sivakumar to deposit YSZ + $Gd_2Zr_2O_7$ composite coatings [48]. Using a suspension instead of a dry powder ensures a more homogeneous dispersion since the size of the micrometric or sub-micrometric solid particles would be better matched to the size of the precipitated clusters of solute precursor produced during spraying. The combination of suspensions and solutions has been very seldom employed in the literature, but the few examples, which include the production of tantalate-based perovskites [49] and of CeO_2-doped TiO_2 photocatalysts [50], are promising. In the field of zirconia-based TBCs, the combined process was investigated by Van Every et al. they dissolved hydrated ytterbium and neodymium nitrates into a suspension of 80 nm diameter 4.5 mol% YSZ powder and ethanol to reduce the thermal conductivity of the coatings [51]. In the same year, the same authors produced rare-earth doped yttria-stabilized zirconia (YSZ) coatings by introducing various dopant pairs (Nd_2O_3/Yb_2O_3, Nd_2O_3/Gd_2O_3, and Gd_2O_3/Yb_2O_3) as nitrates added to the YSZ suspension. The primary objective of the study was to evaluate the thermal conductivity of the coatings, with the findings showing that the coatings doped with Gd_2O_3/Yb_2O_3 exhibited the lowest thermal conductivity [52].

There are various potential advantages in using hybrid SPS/SPPS. One is that, in splats where the in-flight synthesis of the rare earth-doped compound is not complete, which can be expected to exist in a rather stochastic process like plasma spraying, the pre-synthesized 8YSZ powder ensures the absence of free, unstabilized zirconia. For example, t-ZrO_2 was reported in coatings with a nominal $SrZrO_3$ stoichiometry obtained by SPPS [53]. Unstabilized zirconia would create stresses by undergoing phase change during thermal cycling. Another advantage is the combined doping with two cations (Y^{3+} and the rare earth cation), which can provide improved performance over single doping, as mentioned previously. Furthermore, 8YSZ suspensions have already become a commercially available product; therefore, their growing industrial maturity can be harnessed to achieve a faster industrial uptake of the new hybrid method, whilst pure solution precursors have not yet found the same level of initial industrial acceptance. The addition of the precursor salt to the 8YSZ suspension brings much greater flexibility in the choice of overall composition, because different doping amounts can be achieved without the need to pre-synthesize a solid-state powder with fixed stoichiometry. Thus, the composition of the suspension/solution precursor could in principle be tailored to the requirements of each specific application.

However, there is limited information regarding the CMAS resistance, the thermal cycling behavior, and the mechanical properties of rare earth-doped TBCs obtained using this combined technique. To address this gap, seeking to enhance the CMAS resistance of zirconia-based TBCs by liquid feedstock spraying while maintaining the advantageous porous microstructure obtained by SPS, this study examined the deposition of coatings by using an ethanol-based suspension of 8YSZ doped with varying concentrations (0.25 M and 0.50 M) of suitable rare earth element compounds, such as $Gd(NO_3)_3{\cdot}6H_2O$, dissolved in the liquid phase. We provide a comprehensive study of the CMAS and thermal cycling behavior of these coatings, with particular emphasis on the effects of the different amounts of gadolinium nitrate added to the 8YSZ suspension. Moreover, nanoindentation measurements on the monolayer systems were conducted to evaluate the hardness and elastic modulus of the synthesized material, while pillar splitting tests were performed to assess the fracture toughness.

In addition, bilayer coatings were produced, having a conventional 8YSZ bottom layer obtained from a commercial powder. The bottom layer was manufactured with two different architectures: porous (16 % porosity) or dense-vertically cracked (DVC). Both types of bottom layer were deposited via APS. On top of these APS 8YSZ layers, SPS/SPPS coatings with a 0.50 M $Gd(NO_3)_3{\cdot}6H_2O$ concentration in the liquid phase were deposited under the same conditions of the monolayer systems. In a final deposition series, a 0.75 M system was sprayed onto a DVC 8YSZ bottom layer to evaluate the effect of an additional increase in the powder concentration.

2. Materials and methods

2.1. Preparation of the suspension

2.1.1. Solubility & stability test

Preliminary solubility tests were conducted to determine the maximum concentration of $Gd(NO_3)_3{\cdot}6H_2O$ that could be added to an ethanol suspension. Small aliquots of the salt (approximately 1 g) were incrementally added to 5 mL of ethanol at room temperature. Following each addition, the mixture was subjected to continuous magnetic stirring until a clear solution was obtained. This procedure was repeated four times, ultimately yielding a clear, colorless solution with a final Gd $(NO_3)_3{\cdot}6H_2O$ concentration of 2.5 M.

Higher concentrations were not investigated, as the intended additions to the YSZ ethanol suspension were specifically designed to fall within the lower range of 0.25–0.75 M (see 2.2). The final solution was stored under ambient conditions, and no precipitation was observed for up to seven days following the completion of the test.

2.2. Feedstock materials and coating deposition

Feedstock materials were prepared by dissolving $Gd(NO_3)_3{\cdot}6H_2O$ (99.9 % purity; Thermo Fisher Scientific) into a commercial suspension (AuerCoat® YSZ 25E T1, Treibacher Industrie AG, Althofen, Austria) containing 25 wt% of ZrO_2-8 wt.% Y_2O_3 (8YSZ) particles (Dv(50) = 0.78 ± 0.02 μm) in ethanol, following the procedures and maximum concentrations determined in the preliminary tests described in Section 2.1.

In the first series of depositions, feedstock systems with Gd $(NO_3)_3{\cdot}6H_2O$ concentrations of 0.25 M (labelled "D2") and 0.50 M (labelled "D4") with respect to the volume of the liquid phase of the suspension were prepared and sprayed on Hastelloy-X discs to examine the effect of composition on the coating properties. Single-layer coatings were directly applied onto discs with a NiCoCrAlY bond coat, replicating the conditions of a turbine blade. The bond coat was vacuum heat-treated at approximately 1100 °C for 2 h before the topcoat deposition. This heat treatment, which is standard practice in TBC manufacturing for gas turbine components, ensured densification, precipitation of the β-NiAl phase, and metallurgical bonding to the substrate.

In the second series, bilayer coatings were produced with a conventional 8YSZ bottom layer from a commercial powder. Two microstructures were used for the bottom layer: porous (16 % porosity) and dense-vertically cracked (DVC). An agglomerated and sintered powder with a particle size of 46/73/115 μm ($d_{10}/d_{50}/d_{90}$) was used for obtaining the porous microstructure, while a fused and crushed powder with a particle size of 22/35/54 μm ($d_{10}/d_{50}/d_{90}$) was used for the DVC microstructure. A 0.50 M system was then deposited on top of these conventional 8YSZ layers under the same conditions as in the first series. The samples with a porous or a DVC bottom layer were labelled "P400" and "D400", respectively.

In the third series, a 0.75 M system was sprayed onto a DVC 8YSZ bottom layer to evaluate the effect of increasing the powder concentration (label "D600").

A list of all coatings tested is reported in Table 1.

A cascaded plasma torch from Lincotek Equipment S.p.A. was employed to apply the ceramic coatings at Lincotek Rubbiano S.p.A. under industrial processing conditions.

2.3. Nanoindentation testing

Nanoindentation testing was employed to quantitatively assess the mechanical properties of the top layers of the D2, D400, and D600 coatings, in order to assess the effect of the $Gd(NO_3)_3{\cdot}6H_2O$ concentration on the mechanical properties of the deposited material. Measurements were performed using an iNano nanoindenter (KLA Instruments) equipped with a Berkovich diamond tip, under load-controlled conditions up to a maximum applied force of 50 mN. The Continuous Stiffness Measurement (CSM) technique was utilized throughout the tests, operating at a constant indentation strain rate of 0.2 s^{-1}. Prior to each testing, the indenter tip area function and frame compliance were carefully calibrated on a certified fused quartz standard, ensuring traceability and accuracy in the determination of contact areas. For each sample, a minimum of 25 indentations were conducted, providing a minimum spacing of 20 μm between adjacent indents to avoid interaction effects and positioning them to avoid major cracks, intersplats, and surface defects. The average mechanical properties, specifically hardness and elastic modulus, were extracted from the CSM curves at a representative indentation depth of 400 nm. Any outlier responses associated with surface anomalies or premature cracking were systematically excluded from the dataset. All tests were performed at ambient laboratory conditions, and special care was taken to monitor thermal drift, which was maintained below 0.05 nm/s during each measurement sequence.

2.4. Micro-pillar splitting tests

The micro-pillar splitting method was employed to assess the fracture toughness of the top layers of the D2, D400, and D600 coatings locally, again with the purpose of identifying the effect of varying the concentration of $Gd(NO_3)_3{\cdot}6H_2O$ in the feedstock. This technique, initially proposed by Sebastiani et al. [54], relies on the sharp indentation-induced splitting of focused ion beam (FIB) fabricated micro-pillars and enables the extraction of apparent fracture toughness values with high spatial resolution and statistical relevance. The critical splitting load, P_c, at which unstable crack propagation occurs during indentation, is related to the fracture toughness, K_c, through equation (1):

$$K_c = \gamma \frac{P_c}{R^{\frac{3}{2}}} \quad \text{(eq.1)}$$

Table 1
List of the coatings tested.

ID	Architecture	Feedstock material	Solute concentration	Microstructure	Deposition
D2	Monolayer	8YSZ – $Gd(NO_3)_3{\cdot}6H_2O$	0.25 M	Columnar	SPS/SPPS
D4	Monolayer	8YSZ – $Gd(NO_3)_3{\cdot}6H_2O$	0.50 M	Columnar	SPS/SPPS
D400	Top layer	8YSZ – $Gd(NO_3)_3{\cdot}6H_2O$	0.50 M	Columnar	SPS/SPPS
	Bottom layer	8YSZ	–	DVC	APS
P400	Top layer	8YSZ – $Gd(NO_3)_3{\cdot}6H_2O$	0.50 M	Columnar	SPS/SPPS
	Bottom layer	8YSZ	–	Porous	APS
D600	Top layer	8YSZ – $Gd(NO_3)_3{\cdot}6H_2O$	0.75 M	Columnar	SPS/SPPS
	Bottom layer	8YSZ	–	DVC	APS

where R is the pillar radius and γ is a dimensionless geometrical coefficient, calibrated via cohesive zone finite element modeling. While pillar splitting is not the only micro-scale method available for fracture toughness evaluation, it offers distinct advantages in terms of rapid, local probing [55] and the possibility of obtaining statistically significant datasets, which is especially valuable for heterogeneous or porous coatings.

Micro-pillars were fabricated using a ThermoFisher Helios 5CX dual-beam FIB-SEM system. The nominal top diameter of the pillars was set at 4.5 μm, with an aspect ratio (height/diameter) greater or equal to 1 to ensure complete stress relaxation within the milled volume. The fabrication process consisted of two main steps: first, a concentric annular trench was milled around each pillar using a Ga^+ ion beam at an acceleration voltage of 30 kV and a current of 0.48 nA, achieving the isolation of the pillar from the surrounding material. Final polishing to the target diameter and height was subsequently performed at a reduced current of 28 pA to minimize FIB-induced damage and amorphization.

To validate the pillars' actual geometry, a cross-sectional analysis was performed on a representative pillar after fabrication, enabling the direct measurement of the effective diameter, taper angle, and aspect ratio (Fig. 1).

Splitting experiments were conducted using a G200 nanoindenter (KLA Instruments) equipped with a Berkovich diamond tip. The area function of the indenter was again calibrated on a fused quartz reference before each series of tests. The indentations were performed in load-control mode without dynamic CSM oscillation, applying a constant indentation strain rate of 0.05 s^{-1} until unstable crack propagation via displacement burst was reached, corresponding to the pillar splitting. At least 10 pillars per coating condition were tested and analyzed to account for the intrinsic variability of the coatings, including subsurface porosity and crack networks, as shown for instance in Fig. 1D–F.

2.5. CMAS corrosion testing

To simulate CMAS corrosion, a suspension was prepared using reagent-grade MgO, $CaCO_3$, SiO_2 (<325 mesh, Sigma-Aldrich), and Al_2O_3 (Martoxid MR-70, Martinswerk, Bergheim, Germany), mixed in the proportions listed in Table 2 to replicate the composition of silicate deposits found in serviced turbines [14,56]. The oxides were blended with water in a 1:2 wt ratio to form a paste, which was applied to half of the coated disc surfaces (60 mg/cm^2). The samples were then heat-treated in air at 1250 °C for 1 h in a muffle furnace [57].

Table 2
Chemical composition of CMAS.

Oxide	CaO	MgO	Al_2O_3	SiO_2
Concentration (wt.%)	33	7	12	48

2.6. Thermal cycle fatigue testing

An automatic lift furnace was employed to assess the thermal cycling fatigue resistance of all the coated samples. The lift platform was raised into a furnace held isothermally at 1100 °C, and the samples were kept inside the furnace for 50 min. The platform was then lowered and the samples were rapidly cooled to 100 °C using compressed air. The test ended when approximately 20 % of the surface area of the ceramic topcoats was spalled, as determined by visual inspection. For each sample, three thermal cycling test repetitions were performed on as-sprayed top surfaces.

2.7. Chemical and microstructural characterization of the coatings

Both as-sprayed and CMAS-corroded coatings were cold-mounted in epoxy resin, sectioned, and ground using progressively finer silicon carbide abrasive papers (P400, P800, P1000, P2500, P4000 sizes). They were then polished with a 3 μm diamond suspension followed by an oxide polishing suspension containing 60 nm colloidal silica for scanning electron microscopy (SEM) analysis. Cross-sectional SEM imaging was conducted using a Quanta-200 apparatus (FEI-ThermoFisher Scientific, Eindhoven, The Netherlands) equipped with an INCA (Oxford Instruments Analytical, High Wycombe, UK) energy-dispersive X-ray (EDX) detector, while high-resolution observations were performed with a Nova NanoSEM 450 (FEI-ThermoFisher Scientific) featuring a field emission gun (FEG) electron source and a Quantax-200 (Bruker Nano GmbH, Berlin, Germany) EDX detector. To ensure adequate conductivity, samples were sputter-coated with a thin (~10 nm) gold layer. Some analyses performed with the FEG-SEM apparatus were conducted in electron channeling contrast mode to reveal the crystalline grain structure. To maximize the channeling contrast, in this case the surface of the sample was not gold-sputtered, and a low e-beam acceleration voltage (3 kV) was used to reduce the issues associated with electrostatic charge accumulation. The same procedure was applied to analyze the microstructure after thermal cycling and CMAS corrosion tests.

The coating thickness was measured using image analysis software (ImageJ – NIH, Bethesda, Maryland, USA) on secondary electron SEM

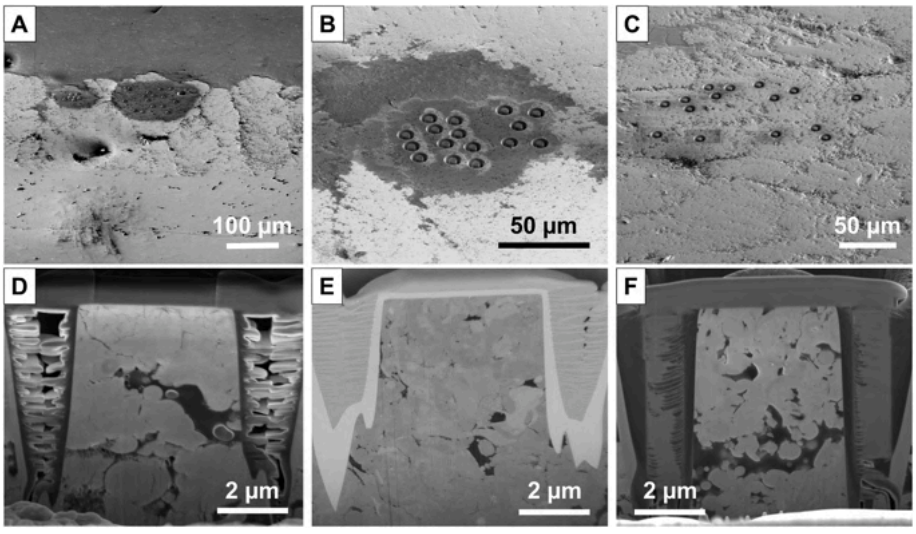

Fig. 1. Representative arrays of pillars on the top layer of samples D2, D400, D600, respectively (A–C); representative cross-sections of the respective pillars to assess their geometrical features (D–F).

micrographs at 200× magnification.

Micro-Raman spectra were collected on the polished cross-sections of as-sprayed and corroded coatings using a LabRam HR Evolution (Horiba, Lille, France) spectrometer. Spectra were acquired with a "green" Nd:YAG solid-state laser ($\lambda = 532$ nm) focused through a 100 × objective as the excitation source, and a 600 g/mm diffraction grating for detection. Additionally, three micro-Raman maps were acquired on large areas of the cross-section of the CMAS-corroded D400 sample, again using the same LabRam HR Evolution spectrometer (Horiba) and solid-state laser ($\lambda = 532$ nm) source, focused through a 10 × objective. Acquisition points were spaced by 4 μm or 5 μm along both the x and y directions on all maps, resulting in total map sizes ranging between approximately 5500 and 10000 points.

The as-sprayed coating surface was scratched to collect particles for analysis with a transmission electron microscope (TEM, Talos F200S, FEI – Thermo Fisher Scientific).

X-Ray Diffraction (XRD) patterns (Empyrean diffractometer, Malvern Panalytical, Almelo, The Netherlands) were obtained on as-sprayed coatings using Cu-Kα radiation emitted from an X-ray tube operated at 40 mA, 40 kV and detected by a 2D array of solid-state detectors (PIXcel3D, Malvern Panalytical). An angular range of $20° \leq 2\theta \leq 85°$ was scanned with a step of 0.0167° and a counting time of 120 s/step.

3. Results and discussions

3.1. As-sprayed monolayer coatings (D2 and D4)

The D2 and D4 samples (Fig. 2) had the typical architecture of a monolayered TBC: a metallic substrate, a NiCoCrAlY bond coat and a top layer with a thickness of 295 ± 34 μm for the D2 sample and 328 ± 17 μm for the D4 sample. The top layer exhibited a "cauliflower-like" columnar structure with high inter-columnar gap density and intra-columnar fine porosity. This is the typical microstructure produced by a liquid feedstock plasma spraying process. However, the columnar in the D4 coating exhibited a more markedly feathery morphology and wider inter-columnar gaps (Fig. 2B), compared to the D2 sample (Fig. 2A). The columnar growth in liquid feedstock spraying is strongly affected by the roughness of the underlying surface, but in this case, the same bond coat was employed; hence, this was likely not the cause in the present case. It can therefore be speculated that a higher concentration of the Gd precursor affected the in-flight behavior of the liquid feedstock, and particularly its fragmentation behavior, altering the size of the resulting droplets. Indeed, if a higher concentration of the Gd precursor resulted in smaller droplets, then such droplets would have been more easily deflected by the stagnation flow in front of the substrate. This resulted in a preferential attachment to the asperities of the target surface, which is the basic mechanism underlying the columnar growth in liquid feedstock spraying, as described in detail by Van Every et al. [58]. It is difficult to obtain a clear assessment of droplet sizes in a liquid feedstock spraying process; however, looking in detail at porous areas

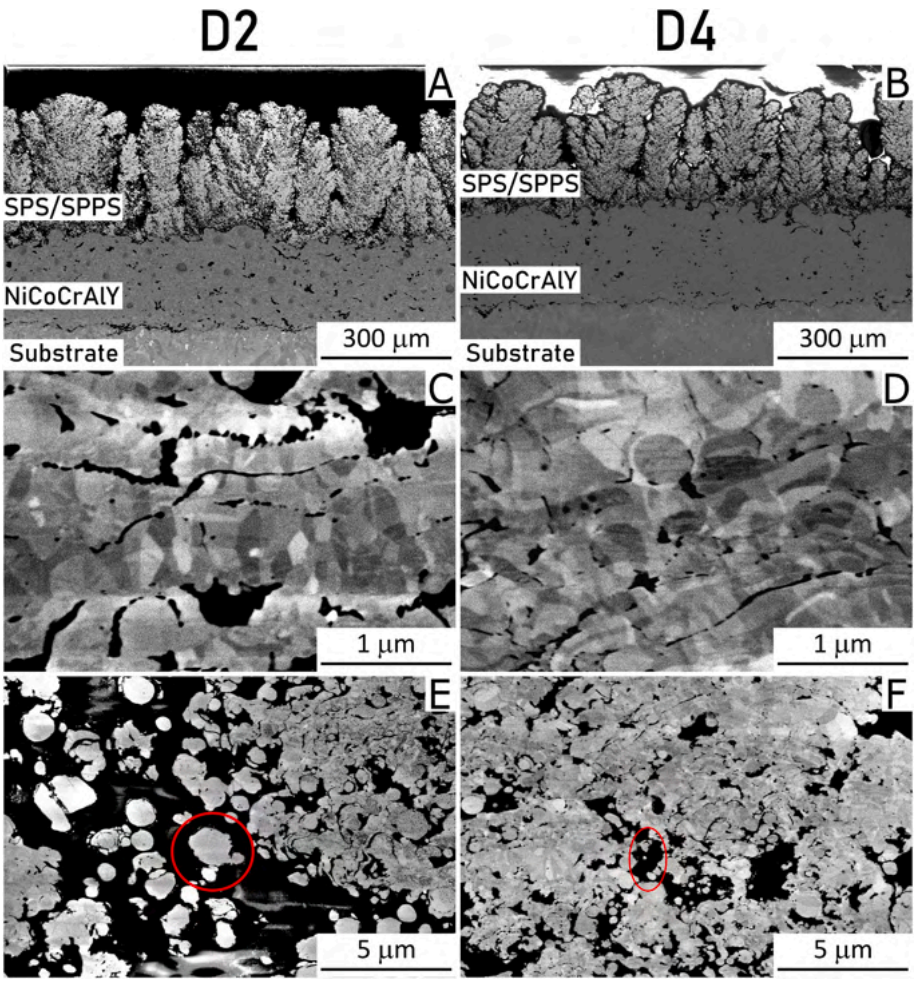

Fig. 2. SEM micrographs acquired on the cross-section of the as-sprayed monolayer coatings D2 (A,C,E) and D4 (B,D,F). Circles in panels E and F indicate non-flattened particles within porous areas.

within the coatings, where non-flattened particles are located, it appears that the D2 sample contains some large particles (>1 μm: Fig. 2E, see the circled area), while the D4 sample contains mostly sub-micrometric rounded particles (Fig. 2F, circle). This observation would therefore confirm the assumption that smaller droplets were produced when the concentration of the Gd precursor increased from 0.25 M to 0.5 M.

Magnified micrographs of the dense parts of the columns show that fully molten splats adhered strongly to one another, as evidenced by the epitaxial growth of columnar grains extending across multiple lamellae (Fig. 2C and D). The heat flux during the deposition process was high enough that it triggered partial sintering of open interlamellar gaps, as evidenced by the presence of some necks bridging across those gaps in Fig. 2C and D. EDX spectra revealed that Gd effectively diffused into the 8YSZ particles during spraying, forming a Y/Gd co-doped zirconia (Fig. 3). Although minor local variations in chemical composition were observed, no regions were composed solely of 8YSZ or of Gd, confirming thorough mixing at the atomic level.

Quantitative EDX analyses conducted on different areas of both samples revealed that increasing the Gd nitrate concentration in the ethanol solvent effectively raised the Gd_2O_3 content in the coatings, from ~11 wt% Gd_2O_3 at 0.25 M concentration to ~18 wt% Gd_2O_3 at 0.50 M.

High-magnification micrographs of the D2 coating show a few bright spots (Fig. 3A–C – spectrum 1), indicating Gd-rich regions. On the other hand, the D4 coating exhibits a more uniform Gd distribution within the splats (Fig. 3B–D). In some areas, unmelted particles rich in Gd were detected (Fig. 3B–D – spectrum 4). TEM analysis on particles scratched from the surface of both top layers was carried out, confirming the coexistence of gadolinium and zirconium and indicating effective elemental integration (Fig. 4).

It is inferred that each lamella originated from an aggregate of several zirconia particles produced when the solvent evaporated from a droplet of liquid feedstock in the plasma jet. The precursor salt precipitated within the interstices among the particles in the aggregates. As the temperature of the aggregate increased, the precursor was first calcined, releasing water and the nitrate groups; then, upon melting of the aggregate, Gd_2O_3 diffused into 8YSZ. This was also confirmed by the fact that lamellae were larger than the 8YSZ particles initially added in the suspension, which had a size of around 0.5 μm.

Fig. 5A displays the Raman spectra of the D2 and D4 coatings. The spectrum obtained from the D2 coating featured a main peak at 600 cm^{-1}, which is characteristic of cubic zirconia. In contrast, the D4 coating revealed two broad bands that can be attributed to the fluorite-type zirconate structure. This suggests that, as the gadolinium nitrate content in the suspension and, hence, in the coating increased, a transformation occurred from the cubic zirconia structure to a disordered fluorite structure, typical of gadolinium zirconate, as expected from the thermodynamic phase diagram of the ZrO_2 – Gd_2O_3 system. This transformation was further supported by the XRD analysis performed on the coatings' surfaces. The XRD pattern of the D4 sample showed a noticeable shift in the 2θ values compared to the D2 sample, indicating a change in the crystal lattice parameter. The lower 2θ values in the D4 coating confirm the presence of the disordered fluorite structure of gadolinium zirconate. These results demonstrate that varying the gadolinium nitrate concentration in the suspension led to a structural transition, which is crucial for understanding the behavior and properties of the coatings.

Notably, the EDX maps acquired by STEM analysis (Fig. 4) show that

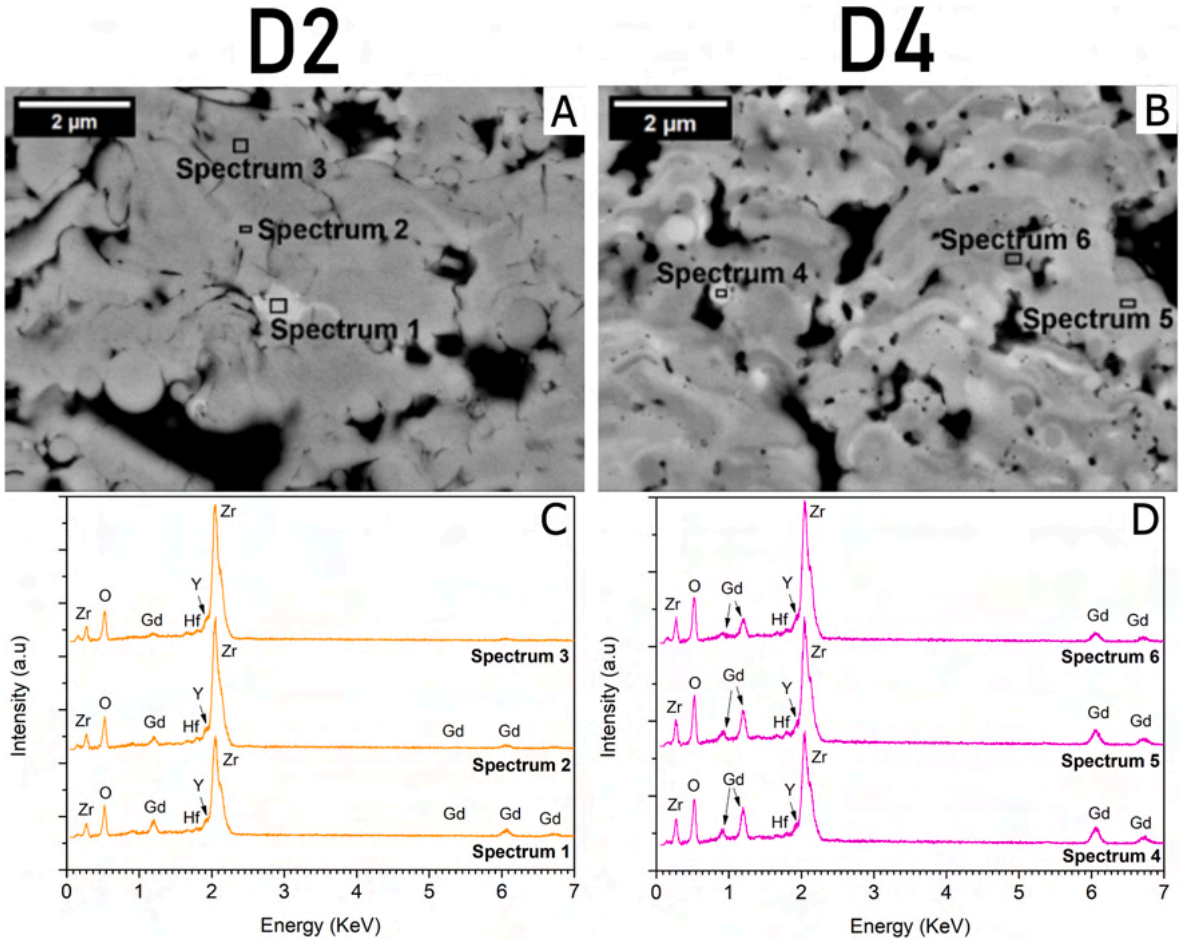

Fig. 3. SEM micrographs and EDX spectra acquired on the cross-section of the as-sprayed monolayer coatings D2 (A,C) and D4 (B,D).

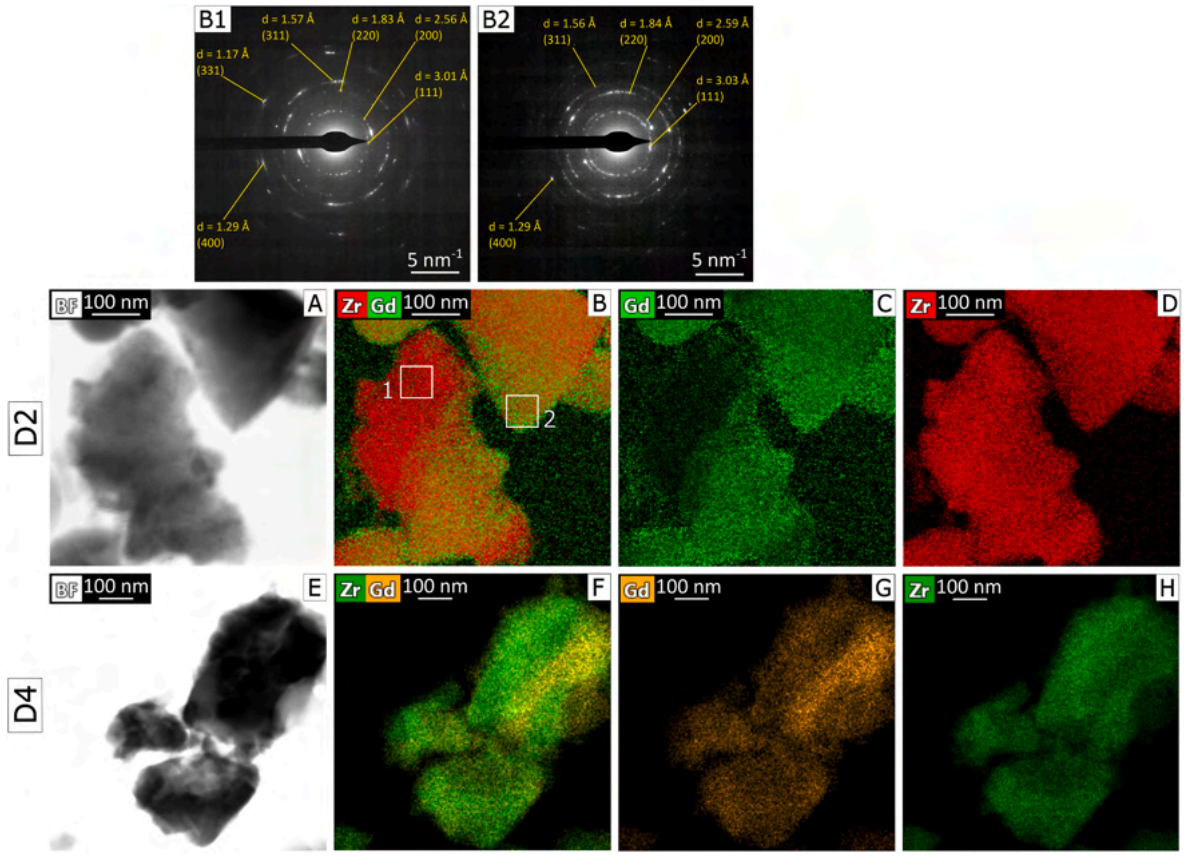

Fig. 4. Bright-field TEM micrographs (A, E) and corresponding elemental distribution maps (B-D; F-H) acquired on fragments detached from the as-sprayed monolayer coatings D2 (A–D) and D4 (E–H). B1 and B2 are FFT patterns relative to areas of sample D2 with low (B1) or high (B2) Gd content.

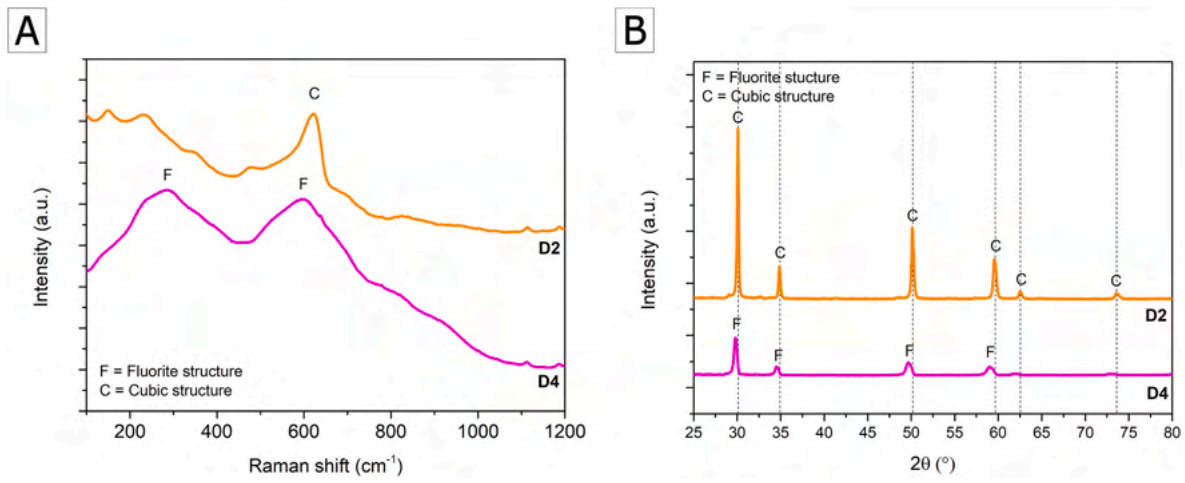

Fig. 5. Micro-Raman spectra (A) and XRD patterns (B) of the as-sprayed monolayer samples D2 and D4.

there were slight local variations in the concentration of Gd, indicating some variability in the degree of interaction between the molten 8YSZ particles and the decomposition products of the Gd precursor, consistent with the previous SEM observations. The selected area electron diffraction (SAED) pattern acquired on a Gd-enriched area of sample D2 (Fig. 4B2) revealed an FCC structure that, compared to an area with less Gd (Fig. 4B1), had slightly larger interplanar spacings, consistent with the fact that an enrichment in Gd modifies the lattice from a cubic zirconia to a fluorite structure, as seen especially clearly in the Raman spectrum of Fig. 5A. Thus, a bit of fluorite phase existed also in the D2 sample, in areas where, due to compositional variability, the Gd content was higher than the average.

3.2. As-sprayed bilayer coatings (D400, P400, and D600)

The samples D400 and P400 (Fig. 6) contained the same amount of Gd-doping in the SPS/SPPS top layer as sample D4, but their architecture differed since they were bilayer systems. To investigate the impact of the bottom layer's microstructure, the two bilayer coatings were designed with identical top layers, but different 8YSZ bottom layers. The P400 coating showed a highly porous bottom layer, whereas the D400 coating had a dense - vertically cracked (DVC) bottom layer. The bottom

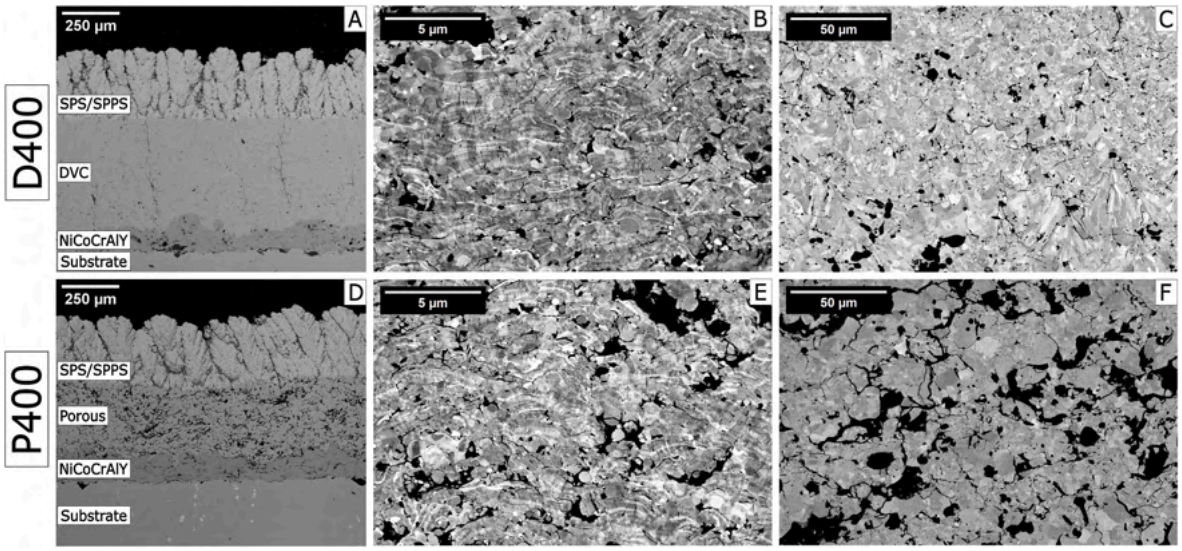

Fig. 6. SEM micrographs of the cross-sections of the as-sprayed bilayer coatings D400 (A, B,C) and P400 (D,E,F). The images were acquired on the SPS + SPPS top layer of both samples (B,E), on the DVC bottom layer of D400 (C), and on the porous bottom layer of P400 (F).

layers differed also for their thickness, as indicated in Table 3, as the porous layer was thinner than the DVC one. Industrially, the DVC layer is not typically used for thin coatings, because the denser microstructure results in higher thermal conductivity, requiring a greater thickness to achieve adequate thermal insulation.

The thickness of the top layers (Table 3) was comparable to the single-layer D4 sample, considering the associated error ranges (Section 3.1). However, the two top layers presented a slightly different cauliflower-like microstructure because of the different roughness of the bottom layer on which they were deposited. In the P400 sample, the feathery columns of the top layers exhibited greater porosity and slightly increased spacing between them, due to the higher roughness of the porous bottom layer (Ra = 5.6 µm) compared to that of the DVC in the D400 sample (Ra = 4.6 µm). Indeed, it is known that the columnar structure originates by the preferential attachment of fine particles to protruding asperities [58]; therefore, the higher the asperity peaks, the more pronounced the columnar growth texture.

The XRD patterns of both the D400 and the P400 samples (Fig. 7B) showed peaks ascribable to the cubic fluorite structure of the gadolinium zirconate of which the top layer is made. This was confirmed by Raman spectra (Fig. 7A), which also exhibited the typical signal of the fluorite structure for the top layers of both samples. Thus, the results confirmed that, as for the D4 sample, Gd was effectively integrated into the 8YSZ lattice. Conversely, Raman spectra acquired on the bottom layer showed characteristic peaks at 150 cm^{-1}, 250 cm^{-1}, 470 cm^{-1} and 640 cm^{-1}, which indicated the presence of tetragonal zirconia.

TEM micrographs acquired on fragments detached from the P400 sample confirmed a very fine-grained microstructure, with individual grains well below 100 nm in size (Fig. 8A). High-resolution views (Fig. 8B and C) showed lattice planes with a spacing consistent with the (111) planes of cubic fluorite. The FFT transform of areas with identifiable lattice planes (Fig. 8D) could also be indexed to an FCC lattice consistent with the fluorite structure.

The D600 sample (Fig. 9) was similar, in terms of architecture, to the D400 one, but an increased amount of Gd in the suspension, having a 0.75 M solute concentration, resulted in a Gd_2O_3 content of approximately 26 wt% in the top layer, as measured by EDX analysis. The top layer thickness was 272 ± 11 µm, which was slightly lower than the D400 sample.

When compared to the Gd_2O_3 levels in the D2 and D4/D400 coatings, the less-than-proportional increase in Gd_2O_3 in the D600 sample suggests some loss of Gd during deposition. This could be due to vaporization and some of the solute not managing to diffuse into the molten 8YSZ particles during the flight period in the plasma stream. It was also noted that the chemical homogeneity of the top layer was worsened in comparison to the D4/D400 samples: magnified backscattered-electron views (Fig. 9B) indeed revealed various greyscale contrast levels, indicative of widely varying contents of Gd in different areas. This means that Gd was probably not evenly distributed across different droplets and/or was vaporized at different rates in different droplets.

Table 3
Thickness of the coating layers measured with the ImageJ software.

	Bottom Layer Thickness (µm)	Top Layer Thickness (µm)
D400	474 ± 25	301 ± 9
P400	305 ± 20	297 ± 15

3.3. Mechanical properties

3.3.1. Nanohardness and elastic modulus

The mechanical response of the top coatings, assessed via nanoindentation, reflected both the evolving chemistry and the microstructural characteristics induced by Gd doping and the hybrid SPS/SPPS process.

As shown in Fig. 10, D400 displayed a higher elastic modulus compared to D2, with non-overlapping standard deviations confirming the increase was statistically meaningful (Table 4). The increase in elastic modulus observed for D400 was consistent with its more uniform and continuous top-layer microstructure. As noted in Section 3.2, indeed, the cross-sectional SEM images (Fig. 6A–C) showed a denser microstructure with reduced interlamellar porosity and well-developed columnar features. The top layer looked finer and more cohesive than in the other coatings, likely due to a more homogeneous in-flight fragmentation and melting of the droplets, which was consistent with the correspondingly more homogeneous incorporation of Gd supported by the Raman spectrum of D400 (see the discussion in Section 3.2).

D600, obtained with a higher precursor concentration (0.75 M), showed a slight decrease in modulus compared to D400, though still within a comparable range. This behavior correlated with the increased variability in local composition seen in backscattered SEM (Fig. 9B). D2, with the lowest Gd content (0.25 M), exhibited the lowest average modulus. Also in this case, the SEM and TEM analyses (Fig. 2C–E, and Fig. 4A–D) showed more evident Gd-rich clusters, suggesting limited

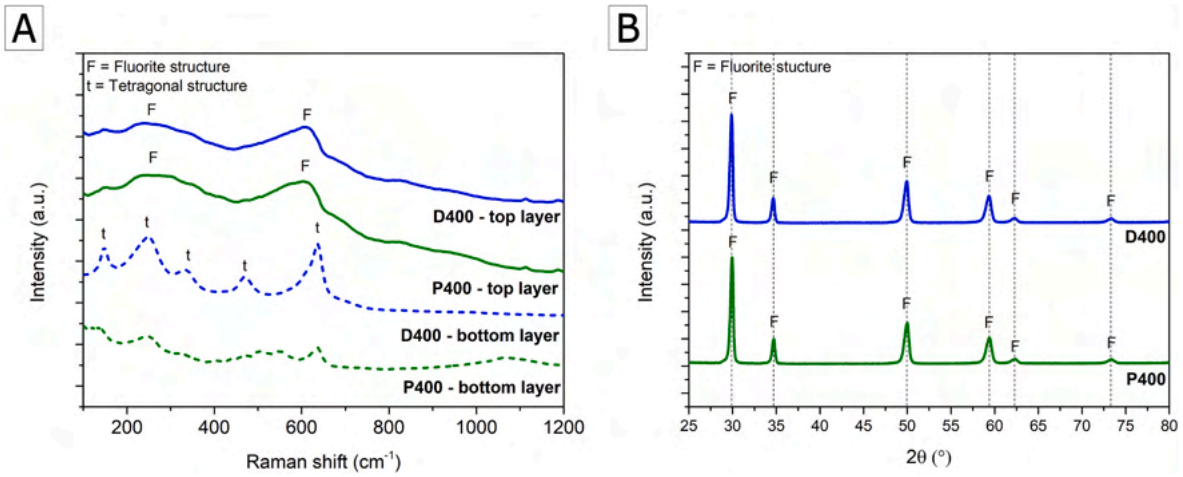

Fig. 7. Micro-Raman spectra (A) and XRD patterns (B) of the as-sprayed bilayer samples D400 and P400.

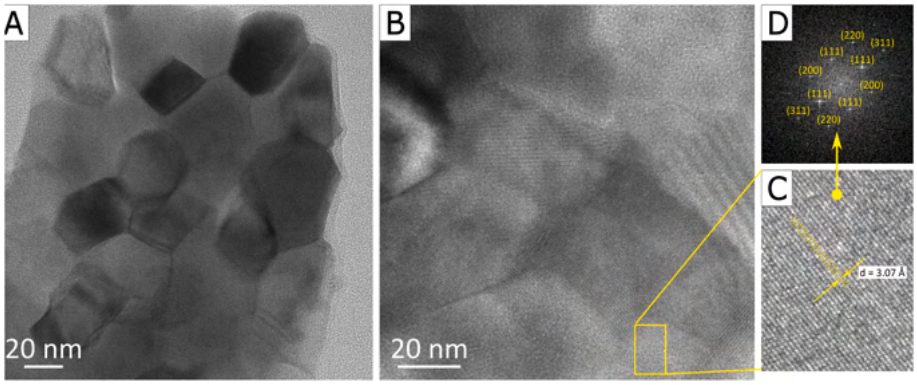

Fig. 8. HR-TEM micrographs of fragments of the P400 sample: overview of a fine-grained area (A) and magnification of the grains (B), with a digitally zoomed-in view of the lattice plains within a grain (C) and the corresponding FFT pattern (D) indexed to an FCC lattice.

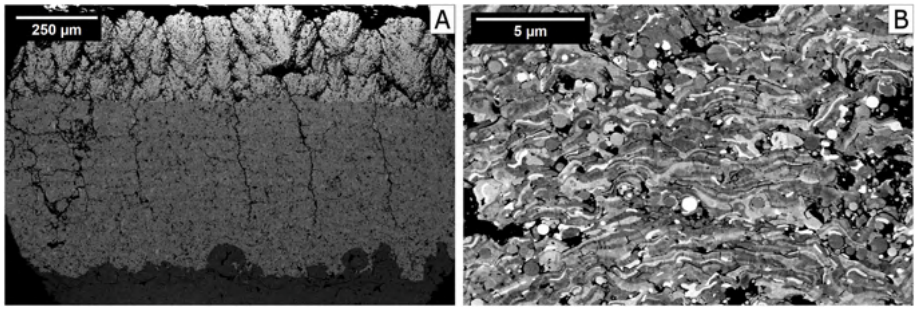

Fig. 9. SEM micrographs of the as-sprayed bilayer coating D600 (A,B). Panel B shows a detailed view of the SPS + SPPS top layer.

incorporation of Gd into the zirconia lattice. Thus, a decrease in elastic modulus correlated in both cases with greater chemical inhomogeneity, probably because both features were caused by a less homogeneous fragmentation and melting of the droplets. The resulting microstructure was therefore more porous and less cohesive, with weaker interlamellar bonding and less efficient stress transfer under indentation. Notably, the elastic moduli of the D400 and D600 samples are lower than the value of ~ 300 GPa reported in Ref. [59] for bulk $Gd_2Zr_2O_7$, although they all exhibited the same fluorite structure. This may indicate that, in fact, the elastic modulus measured by nanoindentation on the coatings is affected not only by the "intrinsic" mechanical properties of the material, but also by the presence of defects (pores, inhomogeneities), corroborating the previous discussion.

Hardness values across the three samples were broadly similar, with overlapping standard deviations indicating no statistically significant differences. This was consistent with the fact that hardness, unlike the elastic modulus, is less sensitive to small compositional or structural variations when the indentation depth is confined to ~400 nm. Accordingly, the hardness values measured on the present samples are consistent (within the respective error ranges) with the value of 10.88 ± 0.89 GPa provided in Ref. [59] or bulk $Gd_2Zr_2O_7$. Indeed, the plastically deformed volume produced in an indentation experiment is much more localized than the elastic deformation field; therefore, while the measured elastic modulus is affected by the microstructure of the sample, the hardness value reflects the "intrinsic" properties of the coating material, irrespective of the defects.

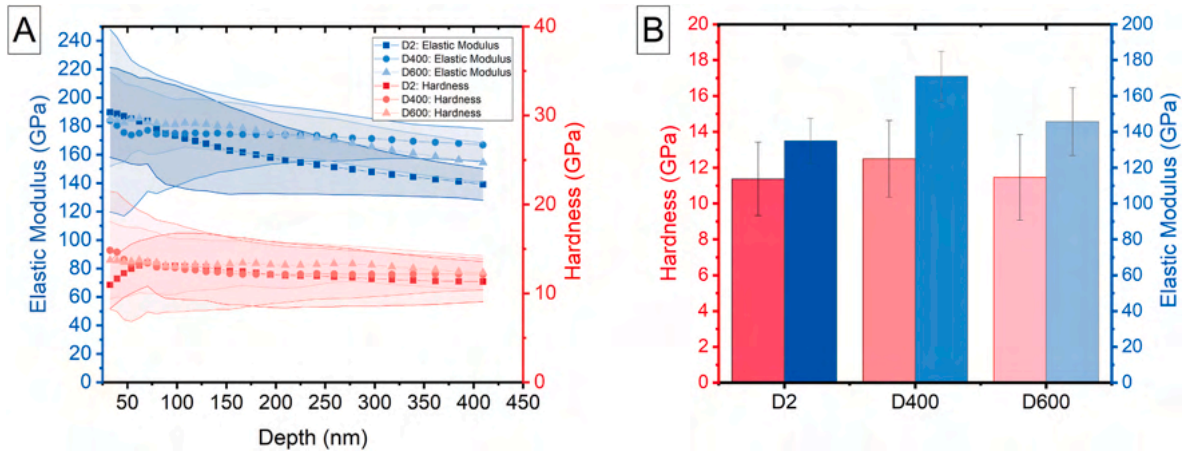

Fig. 10. Mechanical properties measured via CSM nanoindentation: the elastic modulus and hardness measured as a function of the penetration depth (A), and the average values of elastic modulus and hardness extracted at the maximum penetration depth (B).

Table 4
Average values of nanoindentation hardness and elastic modulus were extracted at the maximum penetration depth. Elastic Modulus to Hardness ratio is directly linked to the γ coefficient selection in the fracture toughness measurements of Section 3.3.2.

Sample	Hardness (GPa)	Elastic Modulus (GPa)	E/H
D2	11.4 ± 2.0	135.0 ± 12.5	11.9 ± 2.4
D400	12.5 ± 2.1	171.0 ± 13.8	13.7 ± 2.6
D600	11.4 ± 2.4	145.7 ± 18.9	12.7 ± 3.1

Taken together, the results indicate that the mechanical stiffness of the coatings was increased with Gd doping and its homogeneous integration into the YSZ matrix. However, further increases in solute concentration (as in D600) did not translate into additional increases in elastic modulus and may even lead to microstructural degradation, as suggested by the increased scatter and inhomogeneity in both mechanical and chemical characterization.

3.3.2. *Fracture toughness*

Table 5 reports the apparent fracture toughness of the top layers derived from micro-pillar splitting tests, whose load-displacement curves are illustrated in Fig. 11. All standard deviations overlapped, indicating no statistically significant differences among the coatings.

D400, despite showing the highest elastic modulus in nanoindentation (Section 3.3.1), did not exhibit improved fracture toughness. On the contrary, it showed the widest dispersion in critical load and toughness values. This increased variability was consistent with the presence of sub-surface microstructural features, such as segmentation lines or intra-lamellar defects, visible in the SEM cross-section of the pillar area (Fig. 1B). These heterogeneities influenced the crack initiation and propagation processes, introducing scatter in the fracture response.

The decoupling between stiffness and toughness reflected the different sensitivity of the two measurements: nanoindentation probed the average elastic behavior over a small but continuous volume. At the same time, pillar splitting was controlled by local defects that acted as crack triggers. As similar defect types were present in all samples, especially at sub-surface level, the average fracture resistance remained comparable across the D2, D400, and D600 coatings despite the differences in elastic modulus.

Table 5
Average values and standard errors for the critical splitting load (P_c) and the apparent fracture toughness (K_{IC}).

Sample	P_c [mN]	K_{IC} [MPa•m$^{1/2}$]
D2	11.1 ± 1.6	0.84 ± 0.12
D400	9.2 ± 2.5	0.77 ± 0.21
D600	10.0 ± 1.6	0.80 ± 0.13

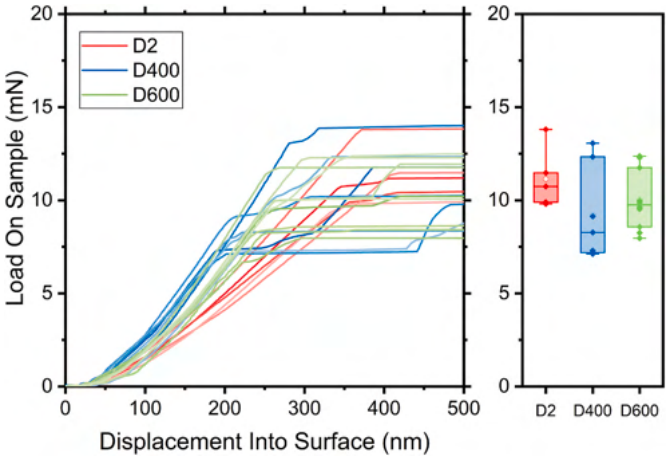

Fig. 11. Indentation curves on pillars show fracture events (displacement bursts) and the distribution of critical loads for the three investigated samples (right).

These values were also notably lower than those measured by the same technique on APS 8YSZ coatings (2.22 ± 0.39 MPa m$^{1/2}$) and even lower than those of APS ZrO_2 – 55 wt% Y_2O_3 (1.43 ± 0.17 MPa m$^{1/2}$) [60]. The difference reflected both the lower intrinsic fracture toughness of a fluorite-type zirconate compared to t`-8YSZ, which has a characteristic ferroelastic toughening mechanism [61], and the more widespread, fine porosity of the liquid feedstock sprayed coatings compared to conventional APS ones, which meant that there was a higher likelihood of having defects within the pillars as compared e.g. to an APS coating made of ZrO_2 – 55 wt% Y_2O_3, which also had a fluorite structure. Accordingly, the coatings also exhibited somewhat lower fracture toughness than bulk $Gd_2Zr_2O_7$ (1.36 ± 0.12 MPa m$^{1/2}$ [59], confirming that the results were likely influenced by tiny defects within the pillar volume.

3.4. *Coatings after CMAS corrosion testing*

3.4.1. *Monolayer coatings*

During the corrosion test, half of the surface of each sample was not covered with the CMAS paste, but it was subjected to the same heat

treatment. After the heating at 1250 °C, sintering and grain growth occurred within all the "hybrid" sprayed top layers in this part of the samples. The splats, which were clearly visible in the SEM micrographs of the as-sprayed coatings (Fig. 2), were no more identifiable. Sintering caused a loss of lamellar structure and polygonal grains resulted from grain growth (Fig. 12B and. 13B), together with the closure of the globular pores.

On the other half of sample D2 (Fig. 12A), where the corrosive paste was deposited, molten CMAS penetrated the inter-columnar gaps, infiltrated the fine intra-columnar porosity, and attacked the boundaries among the very small crystalline grains. No secondary products were found in the D2 sample (Fig. 12C). The CMAS attacked the crystal grains, separating one from the other, but it did not modify their crystalline structure, as demonstrated by the Raman spectra (Fig. 12E), which showed the typical structure of cubic YSZ.

On the contrary, a higher concentration of Gd within the coatings (D4) caused a chemical reaction between the molten CMAS and the coating material. Needle-like crystals (Fig. 13D – red circles) were clearly visible in the half of the D4 sample subjected to the CMAS attack together with globular grains resulting from the grain-boundary attack. The dissolution of the Gd zirconate, therefore, promoted its interaction with the CMAS melt, and resulted in the precipitation of a secondary crystalline phase.

Both the circular structures (Fig. 13E - spectrum 3) and the elongated crystals (Fig. 13E – red circle - spectrum 2) were analyzed by Raman spectroscopy. In the first case the Raman analyses (Fig. 13F – spectrum 3) confirmed that the globular grains were the remainders of the initial coating after grain-boundary dissolution, retaining the fluorite crystal

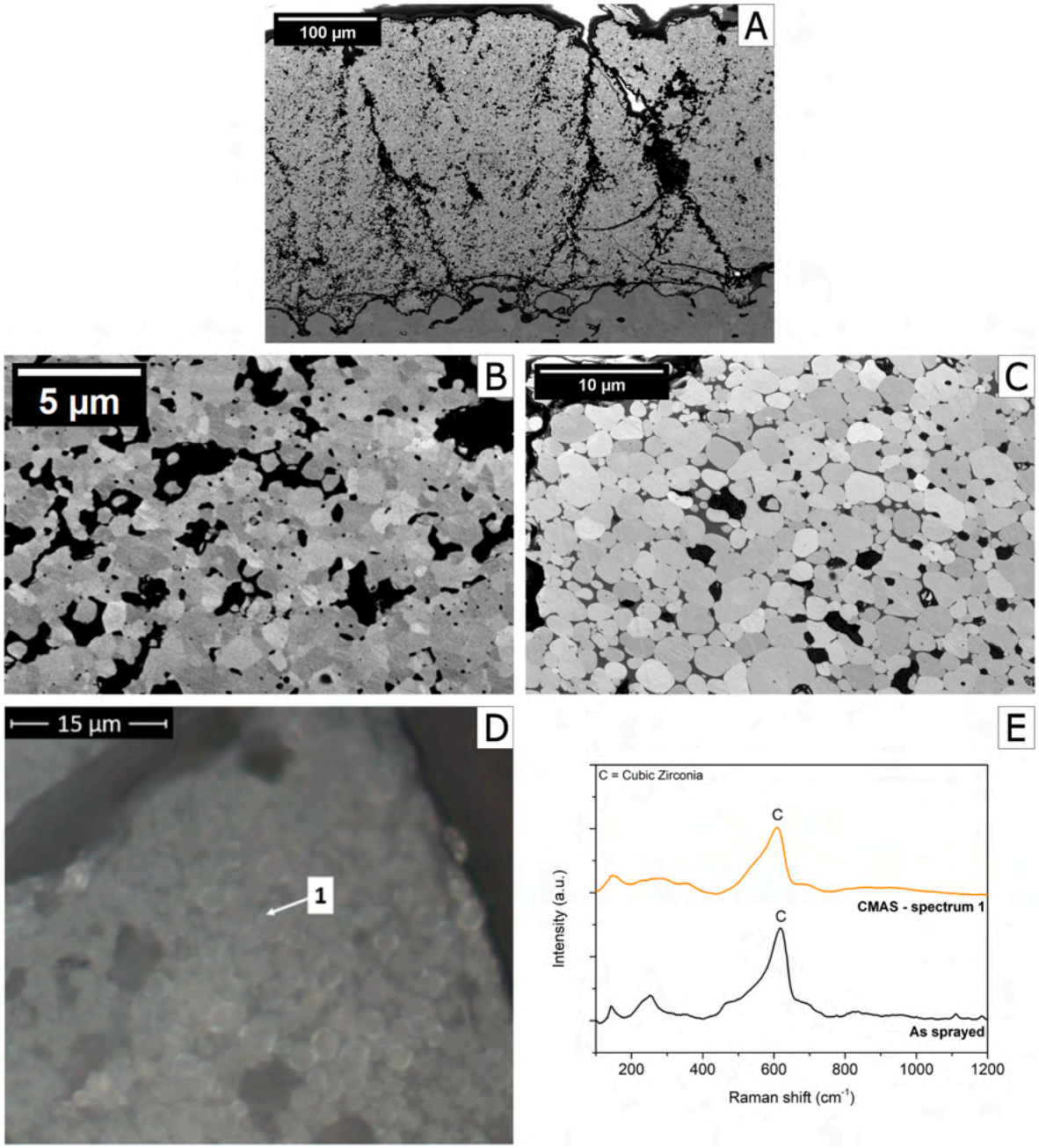

Fig. 12. SEM micrographs of the cross-section of the monolayer coating D2 after corrosion testing (A,B,C): the images were acquired in the area with deposited CMAS (A,C) and the thermally treated area without CMAS deposition (B). Optical micrograph (D) of the same coating after CMAS corrosion testing and corresponding micro-Raman spectrum in comparison to the spectrum of the as-sprayed sample (E).

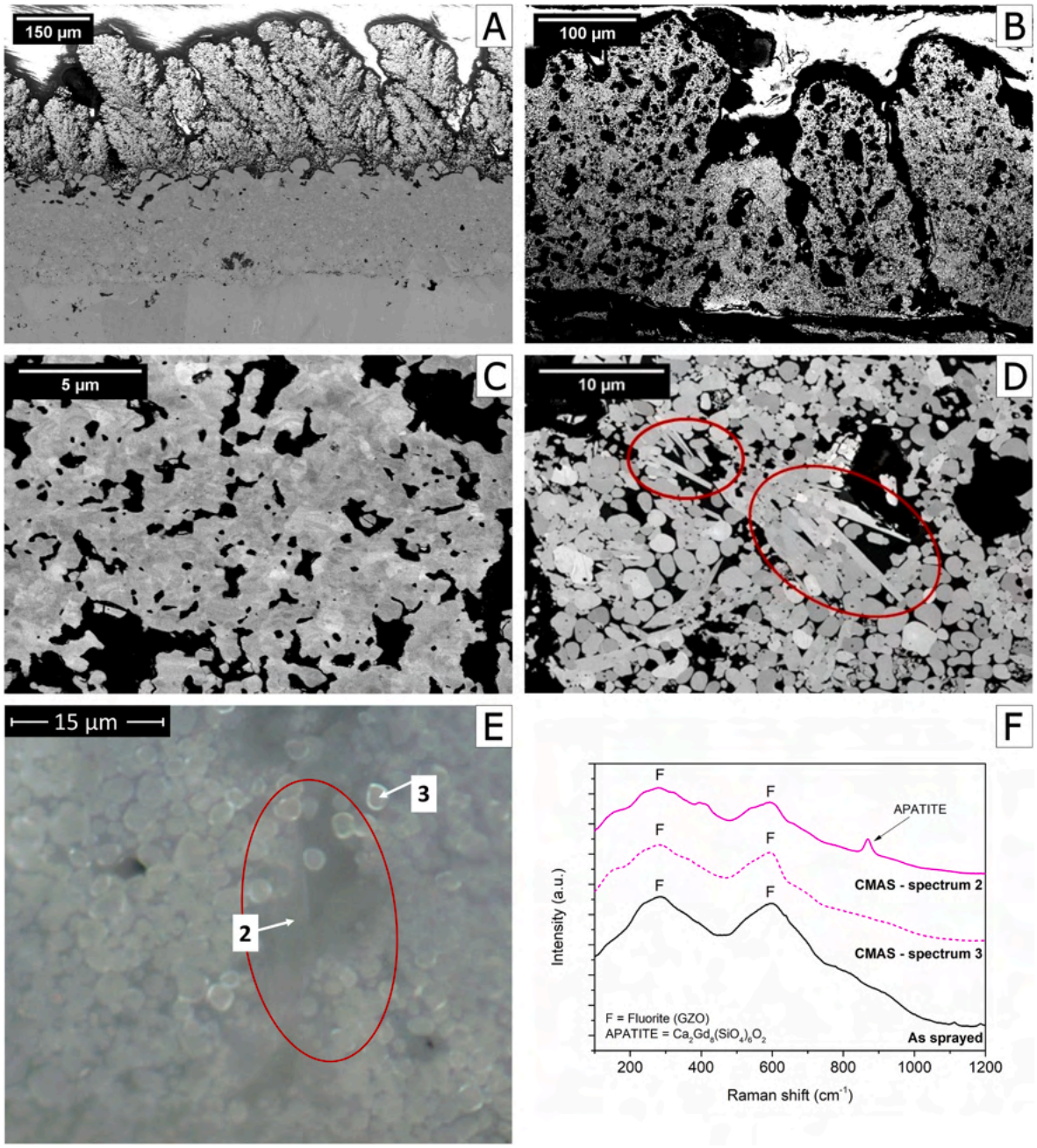

Fig. 13. SEM micrographs of the cross-section of the monolayer coating D4 after CMAS corrosion testing (A,B,C,D): the images were acquired in the area with deposited CMAS (B,D) and the thermally treated area without CMAS deposition (A,C). Optical micrographs (E) of the same coating after CMAS corrosion testing and corresponding micro-Raman spectra in comparison to the spectrum of the as-sprayed sample (F).

structure. In the second case, the Raman spectrum revealed a peak belonging to the apatite phase (Fig. 13F – spectrum 2) in correspondence of the needle-like crystals. These secondary products were, in fact, Gd-apatites ($Ca_2Gd_8(SiO_4)_6O_2$), as also confirmed by the co-existence of Si, Gd and Ca in these areas, as shown by the EDX maps in Fig. 14. They were the product of the reaction between the molten silicates and the dissolved gadolinium zirconate. However, these secondary products were present in too limited quantities to effectively prevent further infiltration of the molten CMAS. As shown in Fig. 13B, the full penetration of CMAS ultimately resulted in complete delamination of the coating at the end of the test.

3.4.2. *Bilayer coatings*

Similar to the single-layer D4 sample, the molten CMAS penetrated deeply into the columnar top layer, filling the inter-columnar spaces and effectively sealing the gaps that once defined the columnar structure. As a result, the microstructure lost its original porous and segmented nature, and appeared as a single, compact block (Fig. 15A). Detailed views (Fig. 15B) once again revealed grain-boundary attack, with the formation of globular grains, and a reaction between the CMAS melt and the dissolved Gd^{3+} to form acicular apatite precipitates (Fig. 15B – red circles).

Furthermore, the top layer exhibited buckling at the interface between the thermally treated section and the area where the corrosive paste was applied (Fig. 15C). The infiltration of CMAS expanded the volume of the top layer and, at the same time, compromised its mechanical strength via the grain-boundary attack. As explained in Section 2.5, the CMAS slurry was applied only onto half of the coated discs;

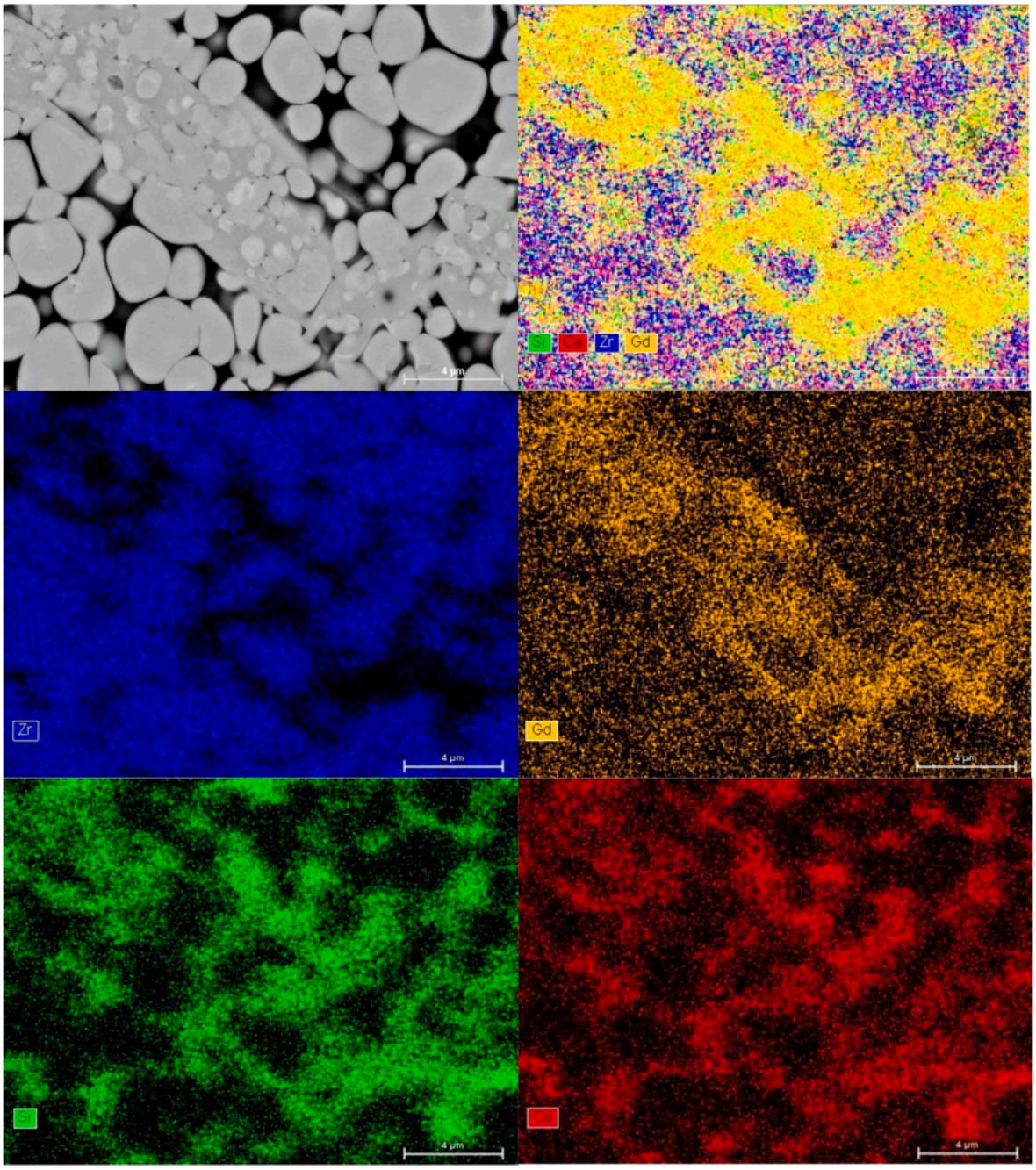

Fig. 14. SEM micrograph and EDX elemental distribution maps acquired on the cross-section of the D4 monolayer sample after corrosion testing in contact with a CMAS melt at 1250 °C for 1 h, showing the formation of Gd,Si-rich phase through interaction between the coating and the CMAS melt.

therefore, during the test, half of each disc was effectively infiltrated by the CMAS melt, whilst the other was just thermally treated at 1250 °C. Because of the additional expansion caused by the CMAS melt, the infiltrated half of the top layer began to buckle at the boundary with the thermally-treated half [62]. Far from this boundary, i.e. well within the infiltrated part of the disc, the overall integrity of the entire TBC system within the CMAS-corroded area appeared intact, despite the corrosion attack (Fig. 15A). EDX analyses indicated that CMAS penetration was mostly limited to the top layer (Fig. 15C and Table 6: spectrum 1). In a large-area EDX analysis, there was no evidence of CMAS elements in the bottom 8YSZ DVC layer (Fig. 15C and Table 6: spectrum 2). The constituents of the CMAS were found only in the segmentation cracks (Fig. 16E), as shown by the results of the EDX analysis (Fig. 15F and Table 6: spectrum 4).

The behavior of the P400 coating was totally different: the larger intercolumnar gaps noted in the top layer (of the P400 sample Section 3.2) made it easier for the CMAS to penetrate to the bottom layer, despite the apatite formation. The bottom layer, in turn, could be infiltrated more easily because of its porous microstructure. In fact, the EDX analyses (Fig. 16E) showed the presence of the silicates not only in the top layer (Spectrum 5 and Spectrum 6), but also within the bottom layer (Spectrum 7). The infiltration of the CMAS in the P400 sample was so severe that it caused the complete failure of the topcoat (Fig. 16A–C) through the cold-shock phenomenon: during cooling, CMAS caused an accumulation of stress because of its low CTE and this resulted in the delamination of the TBC.

Globally, D400 was the coating that performed better under CMAS corrosion attack, because the combined effects of the hindrance to CMAS

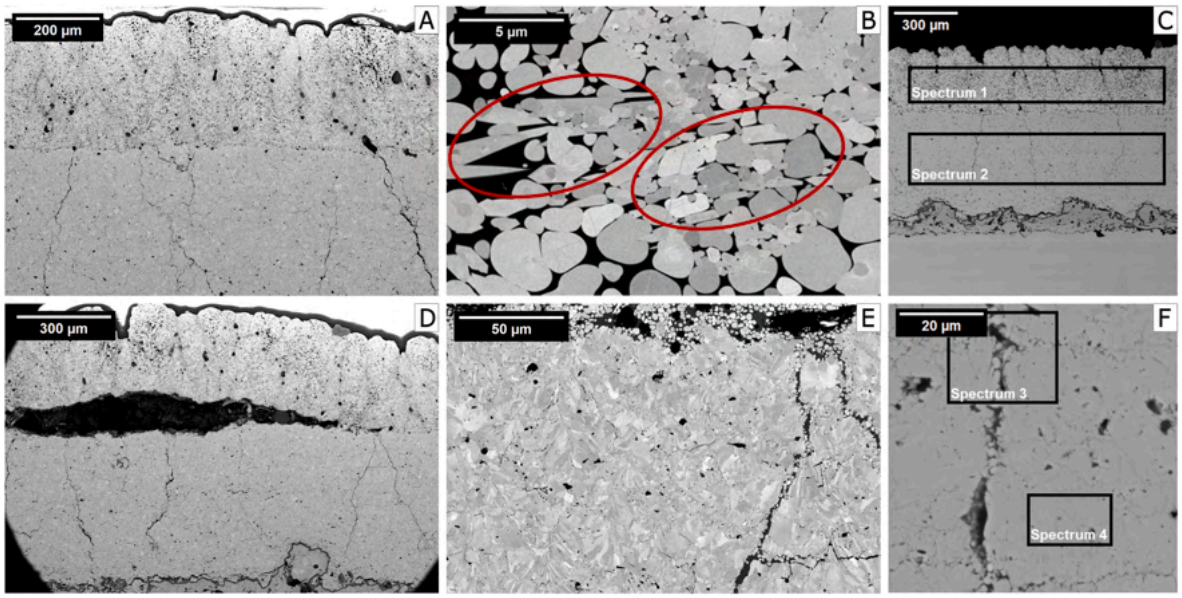

Fig. 15. SEM micrographs of the cross-section of the bilayer coating D400 after CMAS corrosion testing. The images were acquired in the area with deposited CMAS, showing the retained overall integrity of the coating (A), the intergranular attack to the top layer (B) with precipitation of acicular crystals (see circled areas), and some infiltration of CMAS through the segmentation cracks of the DVC 8YSZ bottom layer (E). Image D shows buckling of the top layer at the interface between the area with and without CMAS deposition. Panels C and F show the areas where quantitative EDX spectra were acquired (results in Table 6).

Table 6
EDX quantitative results for the bilayer coatings D400 and P400 after CMAS attack.

Oxide %		Al_2O_3	SiO_2	CaO	Y_2O_3	ZrO_2	Gd_2O_3	HfO_2
D400	Spectrum 1- Fig. 15	2.35	7.4	5.04	3.07	63.0	17.27	1.85
	Spectrum 2 - Fig. 15	–	–	–	6.54	93.08	–	0.37
	Spectrum 3 - Fig. 15	1.02	1.88	1.13	6.43	87.52	–	2.01
	Spectrum 4 - Fig. 15	–	–	–	6.73	90.42	–	2.85
P400	Spectrum 5 - Fig. 16	2.0	13.67	6.34	4.16	57.68	15.21	0.94
	Spectrum 6 -Fig. 16	1.03	7.55	5.82	3.75	63.38	15.5	2.97
	Spectrum 7 - Fig. 16	1.78	5.27	3.3	8.02	79.39	–	2.24

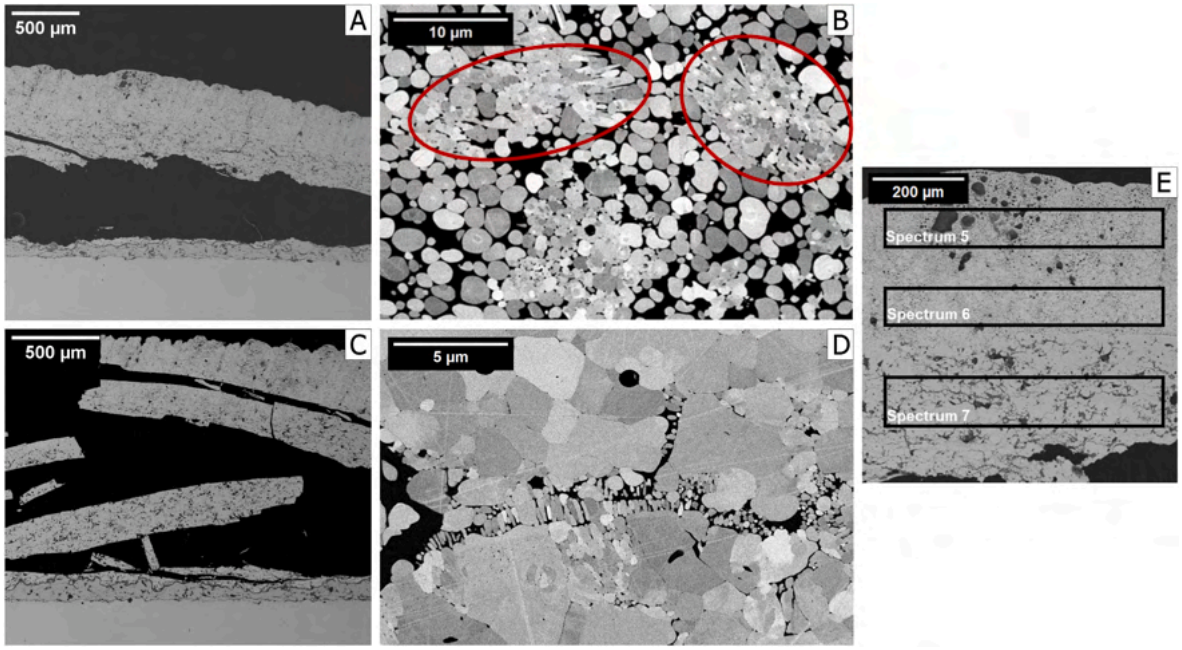

Fig. 16. SEM micrographs of the cross-section of the bilayer coating P400 after CMAS corrosion testing. The images were acquired in the area with deposited CMAS, showing failure of the coating (A,C), intergranular attack and acicular crystals precipitation in the top layer (B), and intergranular corrosion in the bottom layer (D). Panel E shows the areas where quantitative EDX spectra were acquired (results in Table 6).

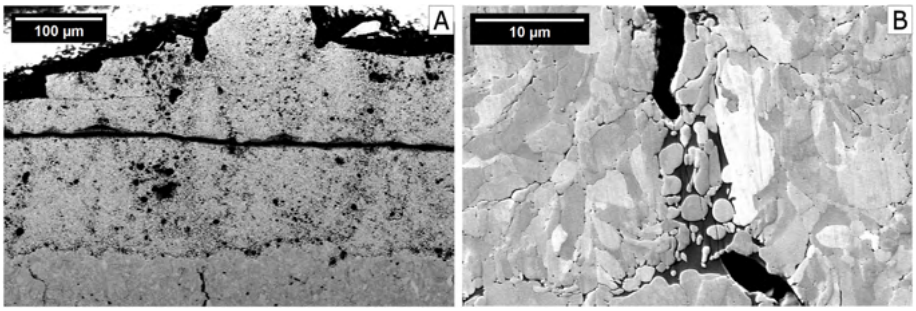

Fig. 17. SEM micrographs acquired on the cross-section of the bilayer coating D600 after CMAS corrosion testing: the images were acquired on the area with deposited CMAS, showing the infiltrated top layer with a longitudinal crack (A) and infiltration of CMAS through the segmentation cracks of the DVC 8YSZ bottom layer, with formation of secondary products (B).

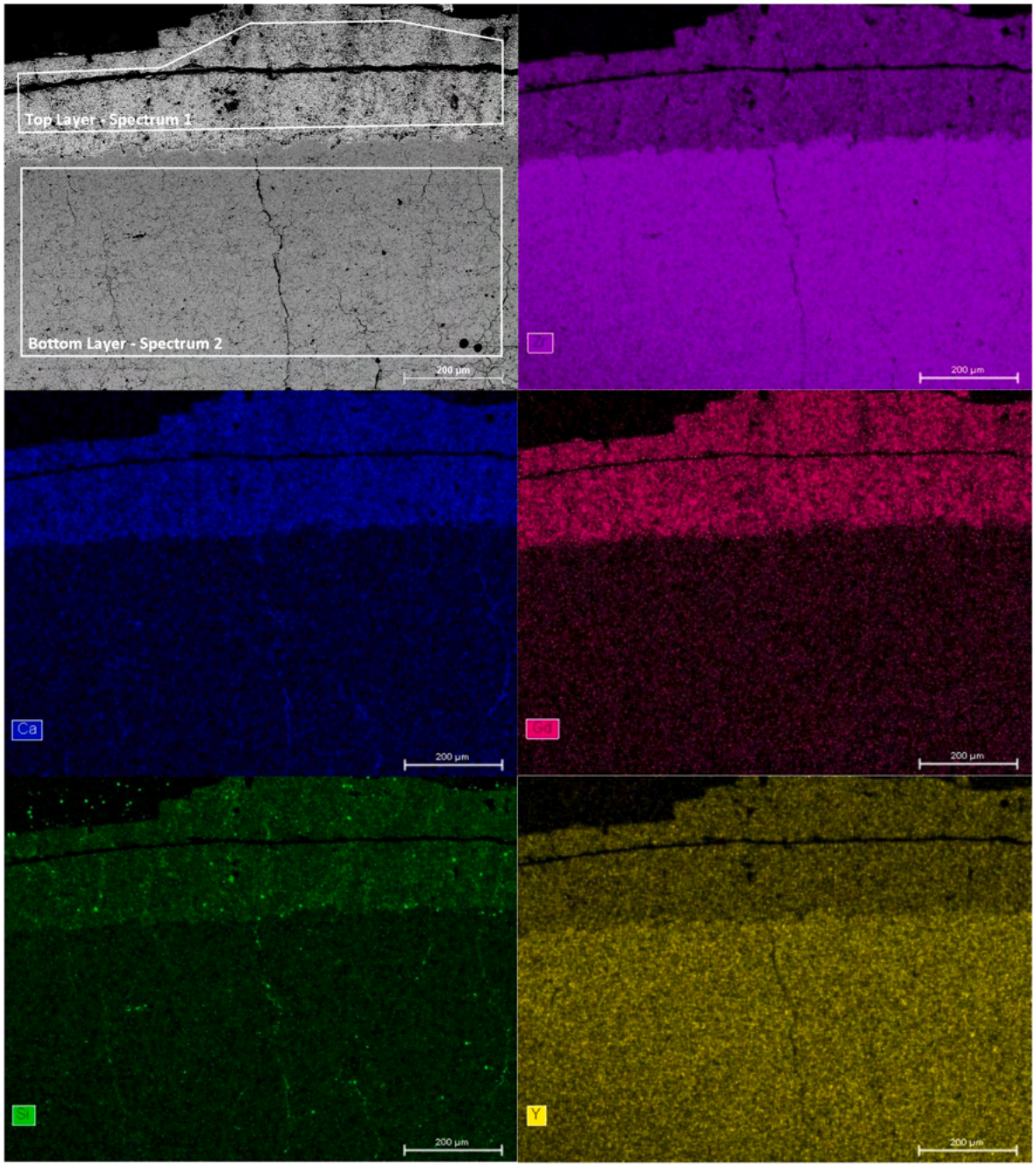

Fig. 18. SEM micrograph and EDX elemental maps (results in Table 7) of the D600 bilayer sample after corrosion testing in contact with a CMAS melt at 1250 °C for 1 h, showing extensive infiltration of the topcoat and some CMAS entering the DVC 8YSZ bottom layer, which was anyway not particularly affected at the macroscale.

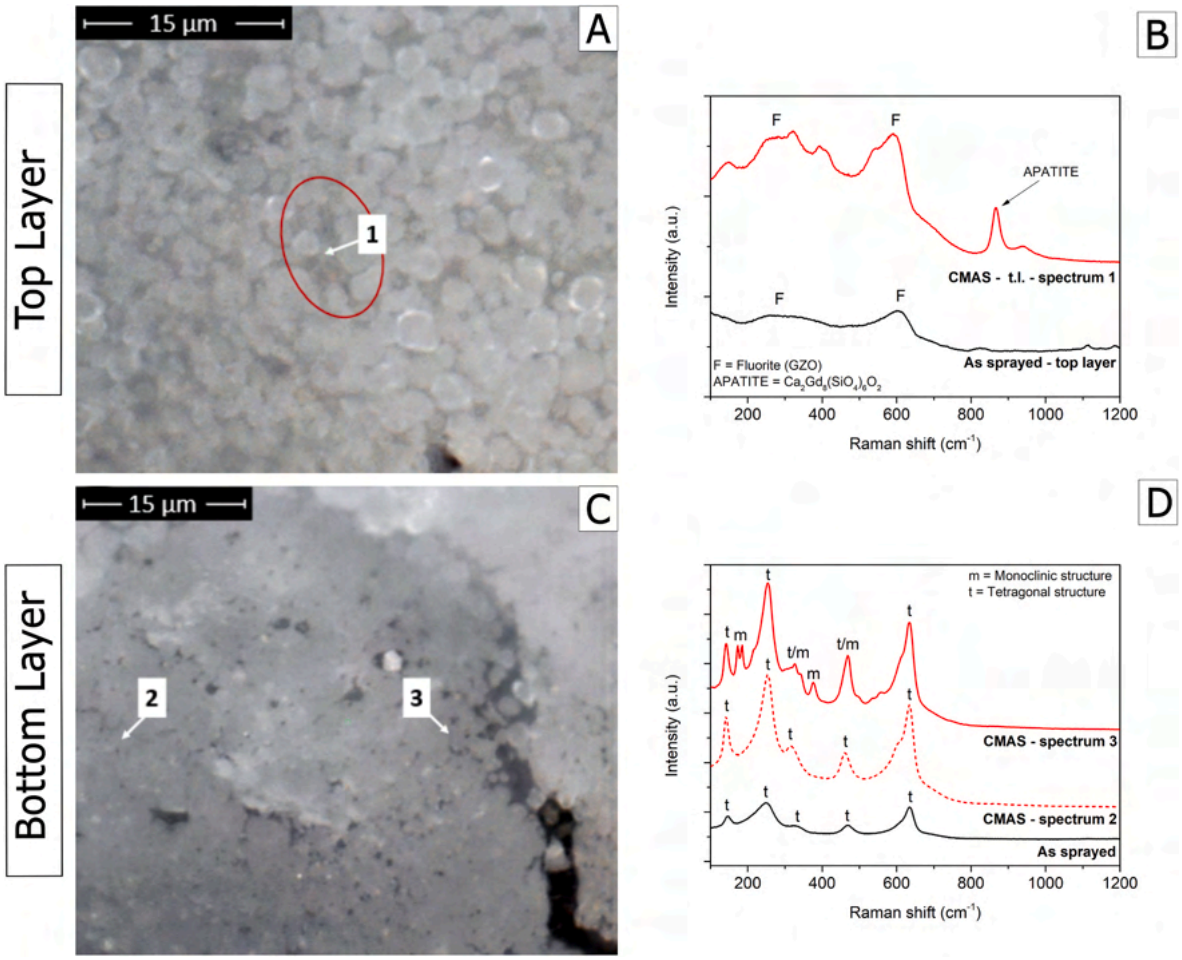

Fig. 19. Optical micrographs (A,C) of the coating D600 after CMAS corrosion testing and corresponding micro-Raman spectra (B,D).

Table 7
EDX quantitative results for the D600 bilayer coating.

Oxide %		Al_2O_3	SiO_2	CaO	Y_2O_3	ZrO_2	Gd_2O_3	HfO_2	MgO
D600	Spectrum 1 - Fig. 18	1.86	6.71	5.1	4.99	58.57	20.99	0.32	1.47
	Spectrum 2 - Fig. 18	0.45	1.11	0.72	7.47	88.98	–	1.08	0.2

penetration due to its chemical interaction with the Gd-zirconate top layer and the denseness of the DVC bottom layer prevented the infiltration of the latter. In this case, it can be concluded that the Gd-zirconate top layer acted as a sacrificial layer and preserved the integrity and functionality of the underlying DVC layer. On the contrary, the porous 8YSZ bottom layer of the P400 sample had a two-fold negative effect. On the one hand, it resulted in wider inter-columnar gaps in the top layer. On the other hand, it was infiltrated more easily by the CMAS melt that made it through the top layer. The result was substantially more severe damage to the entire coating system.

Increasing the concentration of the precursor to 0.75 M, although it increased the Gd_2O_3 content of the topcoat to ~24 wt%, did not produce any further improvement. Rather, it resulted in a loss of deposition efficiency and, therefore, a thinner, less protective top layer under identical deposition conditions (Section 3.2). After CMAS attack, once again, the top layer, which was completely infiltrated by the glassy melt, showed signs of a chemical reaction happening during the corrosion testing. The secondary products were Gd-apatites, the presence of which was demonstrated by the peak around 880 cm^{-1} visible in the Raman spectrum (Fig. 19A and B – red circle - spectrum 1). In this case, however, a longitudinal crack (Fig. 17A) could be seen on the top layer of the coating, which was caused by differential contraction after solidification (cold shock).

The top layer in the D600 sample did act as a sacrificial protection toward the DVC 8YSZ bottom layer, since the molten silicates were mostly stopped at the interface between the two layers. However, the sacrificial protection effect was less marked than for the D400 sample, since the segmentation cracks of the DVC bottom layer (Fig. 17B) were more prominently filled with CMAS. EDX maps indeed revealed elements characteristic of CMAS such as Si and Ca in the segmentation cracks of the DVC bottom layer. Overall EDX analyses acquired on the DVC bottom layer of the D600 also showed detectable amounts of Al, Si, and Ca (Fig. 18 and Table 7), unlike the D400 sample.

Moreover, along the segmentation cracks, globular grains of reprecipitated 8YSZ were visible (Fig. 17B), indicating the interaction of 8YSZ with the CMAS melt that infiltrated the segmentation cracks. Micro-Raman analysis performed on these areas (Fig. 19C and D – spectrum 3) showed peaks around 200 cm^{-1} and 400 cm^{-1}, which indicate the presence of the monoclinic ZrO_2 phase. This transformation demonstrated that the interaction between 8YSZ and the CMAS melt caused the reprecipitation of yttria-depleted zirconia. In areas far from the vertical cracks, the Micro-Raman spectrum did not show any signal from the

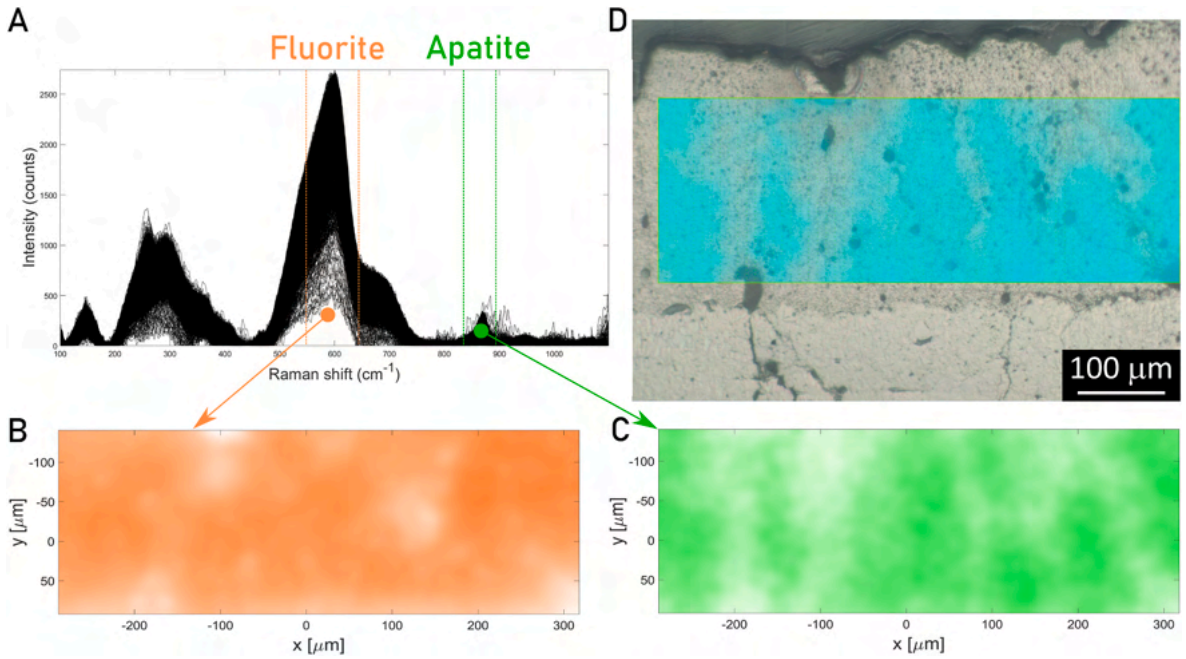

Fig. 20. Micro-Raman mapping of the topcoat in sample D400: overview of all the (background-subtracted) spectra with indication of the regions employed to map the intensity of the fluorite and apatite signals (A), maps of the absolute intensities of the signals of fluorite (B) and apatite (C) plotted using MATLAB (R2024a), and map of the apatite/fluorite intensity ratio superimposed onto the 10 × optical micrograph of the acquisition region (D), with indication of the individual grid points.

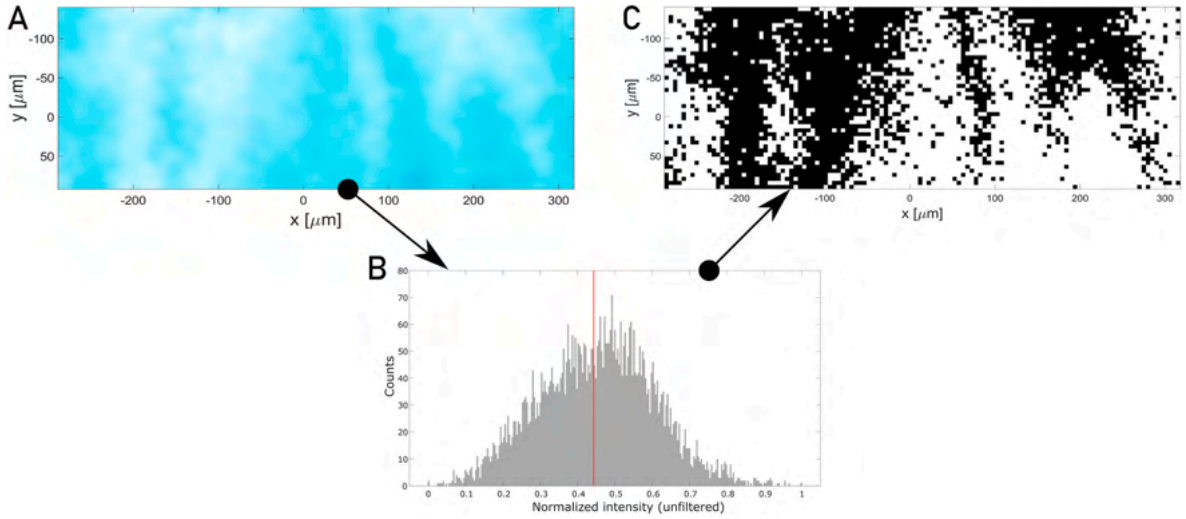

Fig. 21. Map of the apatite/fluorite intensity ratio obtained by micro-Raman mapping (A) and corresponding distribution histogram of the normalized signal intensity, with the threshold identified using Otsu's method in MATLAB R2024a (B) employed to generate a binarized image (C).

monoclinic phase, meaning that the reaction did not proceed in the interior of the 8YSZ DVC layer (Fig. 19C and D – spectrum 2).

In order to characterize in more detail the distribution of the apatite phase in the top layer of the D400 system, which exhibited the best overall performance against CMAS attack, Raman maps were acquired over three large areas on the cross-section of the CMAS-infiltrated region as described in Section 2.7. Specifically, the intensities in the 550-640 cm^{-1} region, indicative of the fluorite phase, and in the 840-885 cm^{-1} region, indicative of the apatite phase, were mapped together with their ratio. As can be seen in the example of Fig. 20, the apatite peak at 870 cm^{-1} was clearly visible in the spectra (Fig. 20A), and apatite was indeed quite widespread across the topcoat (Fig. 20C and D). This result confirms that the formation of apatite was indeed a key factor in hindering the penetration of the CMAS melt, so that, coupled with a dense underlying 8YSZ layer, the system was protected against severe damage.

However, the distribution of apatite was not completely uniform across the topcoat. Indeed, the signal of fluorite was consistently intense across the entire mapped regions (Fig. 20B): its intensity dropped only when the laser beam was focused onto large pores (compare to the micrograph in Fig. 20D), simply because little Raman signal could emerge from those voids. By contrast, the signal of apatite exhibited minima also away from large pores (Fig. 20C). As a result, mapping the ratio between the intensity of the apatite and the fluorite signals (Fig. 20D) reveals that some areas developed less apatite. Superimposing this map onto the original optical micrograph (Fig. 20D) suggests that areas which did not develop apatite were also those that developed more evident signs of frothing, i.e., areas that looked less dense and developed more numerous, tiny pores. This was not true in every case, i.e. sometimes a porous area could be found even when the apatite signal was present, but there was nonetheless a rather close association between

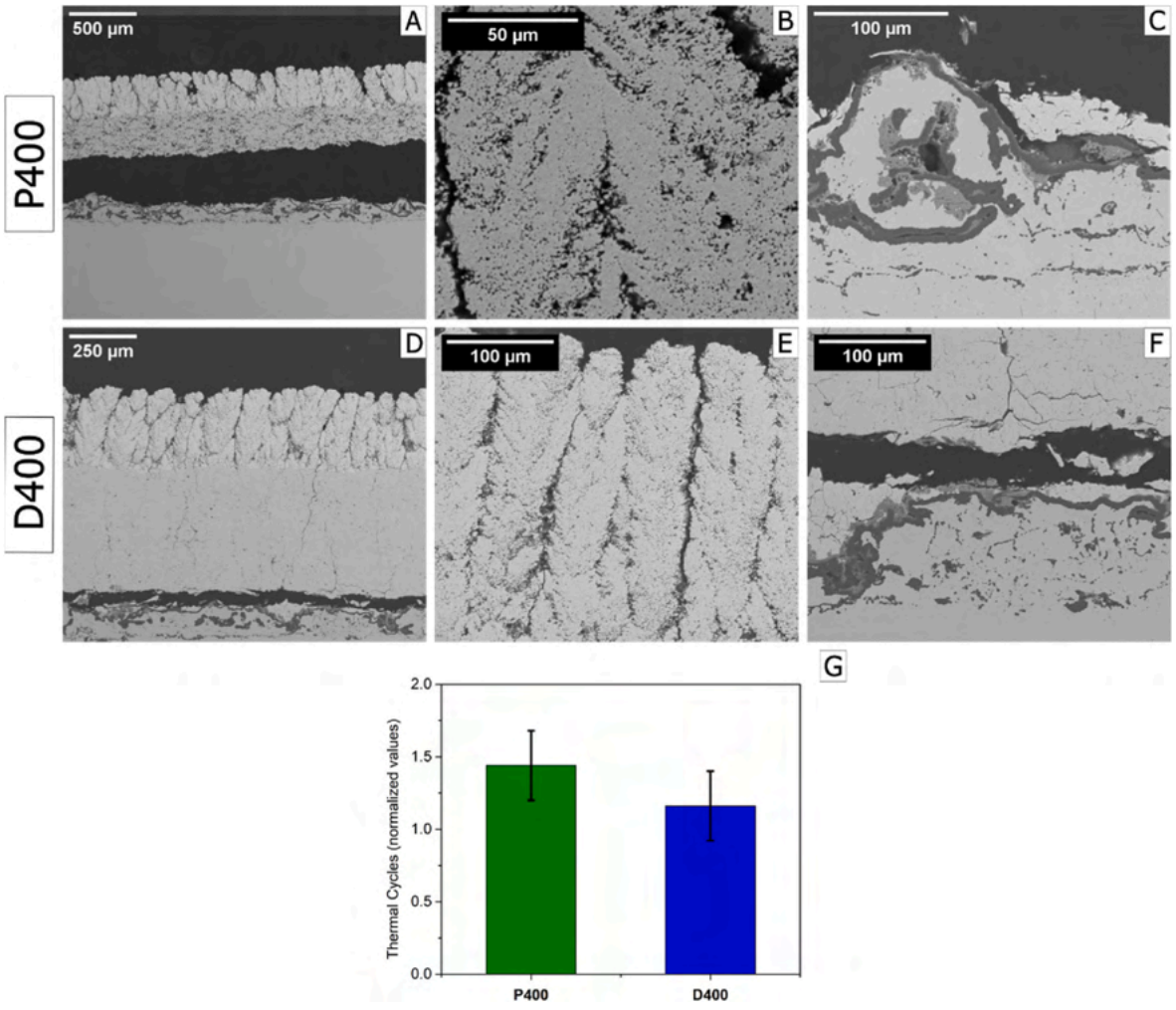

Fig. 22. SEM micrographs of the cross-sections of the coatings after TCF testing: P400 (A–C) and D400 (D–F). Normalized number of thermal cycles to failure for the bilayer coatings D400 and P400 (F).

apatite-lean areas and the tendency to froth. This provides yet more evidence of the importance of apatite formation to limit the penetration of the CMAS melt and maintain the mechanical integrity of the coating. In fact, as seen e.g. in Figs. 15B and 16B, the acicular apatite precipitates bridge between the fluorite grains, countering the intergranular corrosion effect. Where not enough apatite was present, the mechanical integrity of the coating was impaired, and the air entrained in the porosity could expand at high temperatures through viscous flow in the melt.

To quantify the fraction of coating that developed a sufficiently high amount of apatite, an image analysis method was employed. The apatite/fluorite intensity map (re-plotted in Fig. 21A) was binarized (Fig. 21C) using MATLAB R2024a with Otsu's method for thresholding (Fig. 21B). This allows to distinguish areas where the signal of apatite was significant from those where the signal was close to the spectral noise. The area fraction of pixels with intensity above the threshold, averaged over three mapped areas, was (0.51 ± 0.03)%, indicating a good but not optimal ability to develop apatite upon contact with the CMAS melt. This was probably the reason why the same topcoat, when applied onto a porous 8YSZ layer in the P400 system, could not completely prevent the infiltration of the pores in the bottom layer, resulting in the delamination of the system after cooling.

3.5. Coatings after thermal cycling testing

Both the D400 and the P400 samples were subjected to the TCF test and, in both cases, adhesive failure was observed at the interface between the bottom layer and the bond coat (Fig. 22A–D). This indicates that the SPS/SPPS top layer exhibited excellent adhesion to the bottom layer.

The P400 coating demonstrated superior thermal cycling performance when compared to the D400 one. SEM micrographs of the tested samples (Fig. 22B–E) revealed clear signs of sintering in the Gd-zirconate top layer, along with a noticeable increase in thermally grown oxide (TGO) thickness on the bond coat. Specifically, the P400 sample exhibited a TGO thickness of 7.0 ± 0.4 μm (Fig. 22C), while the D400 sample showed a slightly lower value of 5.9 ± 0.3 μm (Fig. 22F). The greater TGO thickness in the P400 coating was directly related to the higher number of thermal cycles it endured before failure.

Since the failure mechanisms of both samples was analogous, the better thermal cycling resistance of the P400 sample was mainly due to the enhanced compliance provided by the greater porosity in the bottom layer and the wider intercolumnar gaps in the top layer. Both of these features played a critical role in relieving the thermal stress during the TCF test, in contrast to the denser microstructure of the D400 coating, which was less capable of accommodating such stress.

Because of its poor performance, the TCF test was not performed on sample D600: the previous analyses showed that it is not suitable for a practical application.

4. Conclusions

In this work, Gadolinium was incorporated into a 8YSZ matrix via a hybrid Suspension/Solution Precursor Plasma Spray (SPS/SPPS) approach. This technique takes advantage of an SPS set-up with the versatility of adding the desired amount of dopant (in this case, Gd) directly to the liquid phase of the 8YSZ suspension. Five different coatings were characterized and tested to investigate the influence of the chemical composition (various concentrations of Gd precursor dissolved in the liquid phase of the 8YSZ suspension) and the architectural configuration (monolayer SPS/SPPS coating or bilayer systems with porous or dense-vertically cracked – DVC – 8YSZ bottom layers) on the functional performance. It was found that.

1) The commercial 8YSZ suspension in ethanol remains stable with the addition of $Gd(NO_3)_3{\cdot}6H_2O$, with the salt being completely soluble in ethanol at all the investigated concentrations (0.25–0.75 M).
2) Increasing the $Gd(NO_3)_3$ concentration in the liquid phase of the 8YSZ suspension from 0.25 M to 0.50 M and 0.75 M resulted in a corresponding increase in the Gd_2O_3 content of the hybrid-sprayed coatings, from ~ 11 wt% to 18 wt% and 24 wt%, respectively. This drove a crystal-structure transition in the deposited coatings: the cubic ZrO_2 phase prevailing at a starting $Gd(NO_3)_3$ concentration of 0.25 M was replaced by the defect-fluorite lattice typical of $Gd_2Zr_2O_7$ at higher concentrations.
3) Microstructurally, the hybrid-sprayed coatings consisted of tapered columns, made of micron-sized lamellae with widespread sub-micrometric porosity.
4) The sample D400, obtained with a starting concentration of Gd $(NO_3)_3$ of 0.50 M and containing ~ 18 wt% Gd_2O_3, showed the highest elastic modulus, because of its more uniform and continuous top-layer microstructure. The coatings obtained with lower (D2) and higher (D600) initial concentration of $Gd(NO_3)_3$ showed greater chemical inhomogeneity and, therefore, resulted in a lower value of E.
5) The average fracture toughness remained comparable, ~ 0.8 MPa $m^{1/2}$, across all these coatings despite the differences in elastic modulus, because of the intrinsic brittleness of the cubic ZrO_2 and the defect-fluorite phases and the presence of microstructural features, such as segmentation lines or intra-lamellar defects, that act as pre-existing cracks during pillar splitting tests.
6) Following CMAS exposure, all the hybrid-sprayed layers were completely infiltrated because of their porosity and the inter-columnar gaps. The layer containing ~ 11 wt% Gd_2O_3 did not exhibit reaction products with the molten CMAS. To the contrary, the coatings with higher Gd content developed some Gd-apatite phases, which slowed down the CMAS penetration. Specifically, the sample containing ~ 24 wt% Gd_2O_3 did not perform any better than the others, because of the aforementioned chemical inhomogeneities of the top layer. Therefore, among all the tested coatings, the one with ~ 18 wt% Gd_2O_3 demonstrated the most effective CMAS resistance.
7) The overall performance of the system during CMAS exposure also depended on the architecture. A DVC 8YSZ bottom layer further blocked the penetration of the CMAS melt that made it through the top layer, whilst a porous 8YSZ bottom layer was readily infiltrated and suffered cold-shock in every case. Thus, the system featuring a top layer with ~ 18 wt% Gd_2O_3 and a DVC 8YSZ bottom layer (sample D400) exhibited the best performance, with the top layer acting as sacrificial protection toward the bottom layer, which was left almost intact.
8) Thermal cycling tests of samples D400 and P400 revealed adhesive failures localized at the interface between the TGO and the underlying 8YSZ bottom layer, indicating the greater adhesion strength between the 8YSZ bottom layers and the SPS/SPPS top layers. Notably, the porous microstructure of the P400 bottom layer conferred enhanced strain compliance, which translated into improved thermal cycling resistance compared to the denser D400 sample.

Overall, these coating systems are promising for applications to industrial gas turbines operating under frequent thermal cycling conditions, with high peak inlet temperatures, in dusty environments. Such combination of conditions, though particularly severe, is becoming increasingly common because high inlet temperatures improve fuel efficiency and reduce CO_2 emissions, and at the same time, gas turbines experience increasingly discontinuous operation cycles as they are employed to compensate for the intermittent power output of renewable energy sources.

CRediT authorship contribution statement

Margherita Cescon: Writing – review & editing, Writing – original draft, Visualization, Methodology, Investigation, Formal analysis. **Stefania Morelli:** Writing – review & editing, Writing – original draft, Visualization, Methodology, Investigation, Formal analysis. **Edoardo Rossi:** Writing – review & editing, Methodology, Investigation, Formal analysis. **Daniele Duranti:** Writing – review & editing, Methodology, Investigation, Formal analysis. **Wenjuan Cheng:** Writing – review & editing, Methodology, Investigation, Formal analysis. **Marco Sebastiani:** Writing – review & editing, Supervision, Project administration, Methodology, Investigation, Funding acquisition, Formal analysis. **Paola Palmero:** Writing – review & editing, Methodology, Investigation, Formal analysis. **Elisa Fiume:** Methodology, Investigation, Formal analysis. **Bartolomeo Coppola:** Methodology, Investigation, Formal analysis. **Alessandro Lanzi:** Methodology, Investigation. **Luca Lusvarghi:** Writing – review & editing, Supervision, Conceptualization. **Giovanni Bolelli:** Writing – review & editing, Visualization, Supervision, Project administration, Methodology, Investigation, Formal analysis, Conceptualization.

Declaration of competing interest

The authors declare that they have no known competing financial interests or personal relationships that could have appeared to influence the work reported in this paper.

Acknowledgements

This work has been supported by the project “CONCERTO – Multiscale modelling/characterization and fabrication of nanocomposite ceramics with improved toughness” funded by the MUR Progetti di Ricerca di Rilevante Interesse Nazionale (PRIN) Bando 2020 - grant 2020BN5ZW9.

References

[1] C.U. Hardwicke, Y.C. Lau, Advances in thermal spray coatings for gas turbines and energy generation: a review, J. Therm. Spray Technol. 22 (2013) 564–576, https://doi.org/10.1007/s11666-013-9904-0.
[2] M.P. Boyce, Advanced Industrial Gas Turbines for Power Generation, Elsevier Masson SAS, 2012, https://doi.org/10.1533/9780857096180.44.
[3] L.G. Bravo, N. Jain, P. Khare, M. Murugan, A. Ghoshal, A. Flatau, Physical aspects of CMAS particle dynamics and deposition in turboshaft engines, J. Mater. Res. 35 (2020) 2249–2259, https://doi.org/10.1557/jmr.2020.234.
[4] R. Naraparaju, U. Schulz, P. Mechnich, P. Döbber, F. Seidel, Degradation study of 7wt.% yttria stabilised zirconia (7YSZ) thermal barrier coatings on aero-engine combustion chamber parts due to infiltration by different CaO-MgO-Al_2O_3-SiO_2 variants, Surf. Coat. Technol. 260 (2014) 73–81, https://doi.org/10.1016/j.surfcoat.2014.08.079.
[5] M.H. Vidal-Setif, N. Chellah, C. Rio, C. Sanchez, O. Lavigne, Calcium-magnesium-alumino-silicate (CMAS) degradation of EB-PVD thermal barrier coatings: characterization of CMAS damage on ex-service high pressure blade TBCs, Surf. Coat. Technol. 208 (2012) 39–45, https://doi.org/10.1016/j.surfcoat.2012.07.074.
[6] P. Mechnich, W. Braue, Solid-state CMAS corrosion of an EB-PVD YSZ coated turbine blade: Zr^{4+} partitioning and phase evolution, J. Am. Ceram. Soc. 98 (2015) 296–302, https://doi.org/10.1111/jace.13241.

[7] D.P.H. Hasselman, L.F. Johnson, L.D. Bentsen, R. Syed, H.L. Lee, M.V. Swain, Thermal diffusivity and conductivity of dense polycrystalline ZrO_2 ceramics: a survey, Am. Ceram. Soc. Bull. 66 (1987) 799–806.

[8] X.Q. Cao, R. Vassen, D. Stoever, Ceramic materials for thermal barrier coatings, J. Eur. Ceram. Soc. 24 (2004) 1–10, https://doi.org/10.1016/S0955-2219(03)00129-8.

[9] R. Vaßen, E. Bakan, D. Mack, S. Schwartz-Lückge, D. Sebold, Y. Jung Sohn, D. Zhou, O. Guillon, Performance of YSZ and $Gd_2Zr_2O_7$/YSZ double layer thermal barrier coatings in burner rig tests, J. Eur. Ceram. Soc. 40 (2020) 480–490, https://doi.org/10.1016/j.jeurceramsoc.2019.10.021.

[10] E. Bohorquez, B. Sarley, J. Hernandez, R. Hoover, L. Tetard, R. Naraparaju, U. Schulz, S. Raghavan, Investigation of the effects of CMAS-infiltration in EB-PVD 7% yttria-stabilized zirconia via Raman spectroscopy, in: AIAA/ASCE/AHS/ASC Structures, Structural Dynamics, and Materials Conference, 2018, 2018, pp. 1–6, https://doi.org/10.2514/6.2018-0096.

[11] S. Krämer, J. Yang, C.G. Levi, C.A. Johnson, Thermochemical interaction of thermal barrier coatings with molten CaO-MgO-Al_2O_3-SiO_2 (CMAS) deposits, J. Am. Ceram. Soc. 89 (2006) 3167–3175, https://doi.org/10.1111/j.1551-2916.2006.01209.x.

[12] G. Pujol, F. Ansart, J.P. Bonino, A. Malié, S. Hamadi, Step-by-step investigation of degradation mechanisms induced by CMAS attack on YSZ materials for TBC applications, Surf. Coat. Technol. 237 (2013) 71–78, https://doi.org/10.1016/j.surfcoat.2013.08.055.

[13] R. Wellman, G. Whitman, J.R. Nicholls, CMAS corrosion of EB PVD TBCs: identifying the minimum level to initiate damage, Int. J. Refract. Metals Hard Mater. 28 (2010) 124–132, https://doi.org/10.1016/j.ijrmhm.2009.07.005.

[14] L. Li, N. Hitchman, J. Knapp, Failure of thermal barrier coatings subjected to CMAS attack, J. Therm. Spray Technol. 19 (2010) 148–155, https://doi.org/10.1007/s11666-009-9356-8.

[15] R. Darolia, Thermal barrier coatings technology: critical review, progress update, remaining challenges and prospects, Int. Mater. Rev. 58 (2013) 315–348, https://doi.org/10.1179/1743280413Y.0000000019.

[16] D.R. Clarke, M. Oechsner, N.P. Padture, Thermal-barrier coatings for more efficient gas-turbine engines, MRS Bull. 37 (2012) 891–898, https://doi.org/10.1557/mrs.2012.232.

[17] N.P. Padture, M. Gell, E.H. Jordan, Thermal barrier coatings for gas-turbine engine applications, Science (1979) 296 (2002) 280–284, https://doi.org/10.1126/science.1068609.

[18] J.B. Huang, W.Z. Wang, Y.J. Li, H.J. Fang, D.D. Ye, X.C. Zhang, S.T. Tu, A novel strategy to control the microstructure of plasma-sprayed YSZ thermal barrier coatings, Surf. Coat. Technol. 402 (2020) 126304, https://doi.org/10.1016/j.surfcoat.2020.126304.

[19] S. Bose, in: Butterworth- Heinemann (Ed.), High Temperature Coatings, Elsevier, Oxford, United Kingdom, 2007, https://doi.org/10.1016/B978-0-7506-8252-7.X5000-8.

[20] L. Pawlowski, Suspension and solution thermal spray coatings, Surf. Coat. Technol. 203 (2009) 2807–2829, https://doi.org/10.1016/j.surfcoat.2009.03.005.

[21] S. Morelli, V. Testa, G. Bolelli, O. Ligabue, E. Molinari, N. Antolotti, L. Lusvarghi, CMAS corrosion of YSZ thermal barrier coatings obtained by different thermal spray processes, J. Eur. Ceram. Soc. 40 (2020) 4084–4100, https://doi.org/10.1016/j.jeurceramsoc.2020.04.058.

[22] A. Joulia, G. Bolelli, E. Gualtieri, L. Lusvarghi, S. Valeri, M. Vardelle, S. Rossignol, A. Vardelle, Comparing the deposition mechanisms in suspension plasma spray (SPS) and solution precursor plasma spray (SPPS) deposition of yttria-stabilised zirconia (YSZ), J. Eur. Ceram. Soc. 34 (2014) 3925–3940, https://doi.org/10.1016/j.jeurceramsoc.2014.05.024.

[23] N.P. Padture, K.W. Schlichting, T. Bhatia, A. Ozturk, B. Cetegen, E.H. Jordan, M. Gell, S. Jiang, T.D. Xiao, P.R. Strutt, E. García, P. Miranzo, M.I. Osendi, Towards durable thermal barrier coatings with novel microstructures deposited by solution-precursor plasma spray, Acta Mater. 49 (2001) 2251–2257, https://doi.org/10.1016/S1359-6454(01)00130-6.

[24] A. Guignard, G. Mauer, R. Vaßen, D. Stöver, Deposition and characteristics of submicrometer-structured thermal barrier coatings by suspension plasma spraying, J. Therm. Spray Technol. 21 (2012) 416–424, https://doi.org/10.1007/s11666-012-9762-1.

[25] P. Fauchais, R. Etchart-Salas, V. Rat, J.F. Coudert, N. Caron, K. Wittmann-Ténèze, Parameters controlling liquid plasma spraying: solutions, sols, or suspensions, J. Therm. Spray Technol. 17 (2008) 31–59, https://doi.org/10.1007/s11666-007-9152-2.

[26] R. Rampon, O. Marchand, C. Filiatre, G. Bertrand, Influence of suspension characteristics on coatings microstructure obtained by suspension plasma spraying, Surf. Coat. Technol. 202 (2008) 4337–4342, https://doi.org/10.1016/j.surfcoat.2008.04.006.

[27] O. Marchand, L. Girardot, M.P. Planche, P. Bertrand, Y. Bailly, G. Bertrand, An insight into suspension plasma spray: injection of the suspension and its interaction with the plasma flow, J. Therm. Spray Technol. 20 (2011) 1310–1320, https://doi.org/10.1007/s11666-011-9682-5.

[28] G. Bertolissi, C. Chazelas, G. Bolelli, L. Lusvarghi, M. Vardelle, A. Vardelle, Engineering the microstructure of solution precursor plasma-sprayed coatings, J. Therm. Spray Technol. 21 (2012) 1148–1162, https://doi.org/10.1007/s11666-012-9789-3.

[29] D. Chen, E.H. Jordan, M. Gell, Effect of solution concentration on splat formation and coating microstructure using the solution precursor plasma spray process, Surf. Coat. Technol. 202 (2008) 2132–2138, https://doi.org/10.1016/j.surfcoat.2007.08.077.

[30] E.H. Jordan, L. Xie, M. Gell, N.P. Padture, B. Cetegen, A. Ozturk, J. Roth, T.D. Xiao, P.E.C. Bryant, Superior thermal barrier coatings using solution precursor plasma spray, J. Therm. Spray Technol. 13 (2004) 57–65, https://doi.org/10.1361/10599630418121.

[31] L. Łatka, A. Cattini, L. Pawłowski, S. Valette, B. Pateyron, J.P. Lecompte, R. Kumar, A. Denoirjean, Thermal diffusivity and conductivity of yttria stabilized zirconia coatings obtained by suspension plasma spraying, Surf. Coat. Technol. 208 (2012) 87–91, https://doi.org/10.1016/j.surfcoat.2012.08.014.

[32] X. Ma, F. Wu, J. Roth, M. Gell, E.H. Jordan, Low thermal conductivity thermal barrier coating deposited by the solution plasma spray process, Surf. Coat. Technol. 201 (2006) 4447–4452, https://doi.org/10.1016/j.surfcoat.2006.08.095.

[33] H. Fang, W. Wang, J. Huang, Y. Li, D. Ye, Corrosion behavior and thermos-physical properties of a promising Yb_2O_3 and Y_2O_3 co-stabilized ZrO_2 ceramic for thermal barrier coatings subject to calcium-magnesium-aluminum-silicate (CMAS) depositio, Corros. Sci. 182 (2021), https://doi.org/10.1016/j.corsci.2020.109230.

[34] L. Guo, M. Li, C. Yang, C. Zhang, L. Xu, F. Ye, C. Dan, V. Ji, Calcium-magnesium-alumina-silicate (CMAS) resistance property of $BaLn_2Ti_3O_{10}$ (Ln=La, Nd) for thermal barrier coating applications, Ceram. Int. 43 (2017) 10521–10527, https://doi.org/10.1016/j.ceramint.2017.05.107.

[35] Z.G. Liu, J.H. Ouyang, Y. Zhou, J. Li, X.L. Xia, $Ln_{0.9}Gd_{0.05}Yb_{0.05})2Zr_2O_7$ ceramics with pyrochlore structure as thermal barrier oxides, Adv. Eng. Mater. 10 (2008) 754–758, https://doi.org/10.1002/adem.200800079.

[36] S. Morelli, S. Bursich, V. Testa, G. Bolelli, A. Miccichè, L. Lusvarghi, CMAS corrosion and thermal cycling fatigue resistance of alternative thermal barrier coating materials and architectures: a comparative evaluation, Surf. Coating. Technol. (2022), https://doi.org/10.1016/j.surfcoat.2022.128433.

[37] M.P. Schmitt, J.L. Stokes, B.L. Gorin, A.K. Rai, D. Zhu, T.J. Eden, D.E. Wolfe, Effect of Gd content on mechanical properties and erosion durability of sub-stoichiometric $Gd_2Zr_2O_7$, Surf. Coat. Technol. 313 (2017) 177–183, https://doi.org/10.1016/j.surfcoat.2016.12.045.

[38] F. Perrudin, C. Rio, M.H. Vidal-Sétif, C. Petitjean, P.J. Panteix, M. Vilasi, Gadolinium oxide solubility in molten silicate: dissolution mechanism and stability of $Ca_2Gd_8(SiO_4)_6O_2$ and $Ca_3Gd_2(Si_3O_9)_2$ silicate phases, J. Eur. Ceram. Soc. 37 (2017) 2657–2665, https://doi.org/10.1016/j.jeurceramsoc.2017.02.022.

[39] S. Krämer, J. Yang, C.G. Levi, Infiltration-inhibiting reaction of gadolinium zirconate thermal barrier coatings with CMAS melts, J. Am. Ceram. Soc. 91 (2008) 576–583, https://doi.org/10.1111/j.1551-2916.2007.02175.x.

[40] R.W. Jackson, E.M. Zaleski, B.T. Hazel, M.R. Begley, C.G. Levi, Response of molten silicate infiltrated Gd2Zr2O7 thermal barrier coatings to temperature gradients, Acta Mater. 132 (2017) 538–549, https://doi.org/10.1016/j.actamat.2017.03.081.

[41] Z. Tian, J. Zhang, L. Zheng, W. Hu, X. Ren, Y. Lei, J. Wang, General trend on the phase stability and corrosion resistance of rare Earth monosilicates to molten calcium–magnesium–alumino silicate at 1300 °C, Corros. Sci. 148 (2019) 281–292, https://doi.org/10.1016/j.corsci.2018.12.032.

[42] A.R. Krause, B.S. Senturk, H.F. Garces, G. Dwivedi, A.L. Ortiz, S. Sampath, N. P. Padture, $2ZrO_2{\cdot}Y_2O_3$ thermal barrier coatings resistant to degradation by molten CMAS: part I, optical basicity considerations and processing, J. Am. Ceram. Soc. 97 (2014) 3943–3949, https://doi.org/10.1111/jace.13210.

[43] C. Wang, Y. Wang, L. Wang, G. Hao, X. Sun, F. Shan, Z. Zou, Nanocomposite Lanthanum zirconate thermal barrier coating deposited by suspension plasma spray process, J. Therm. Spray Technol. 23 (2014) 1030–1036, https://doi.org/10.1007/s11666-014-0068-3.

[44] S. Mahade, N. Curry, S. Björklund, N. Markocsan, P. Nylén, Thermal conductivity and thermal cyclic fatigue of multilayered $Gd_2Zr_2O_7$/YSZ thermal barrier coatings processed by suspension plasma spray, Surf. Coat. Technol. 283 (2015) 329–336, https://doi.org/10.1016/j.surfcoat.2015.11.009.

[45] K. Leng, A.R. Romero, N. Curry, T. Hussain, Multilayer GZ/YSZ thermal barrier coating from suspension and solution precursor plasma spray, Ceram. Int. 50 (2024) 631–649, https://doi.org/10.1016/j.ceramint.2023.10.142.

[46] C. Jiang, E.H. Jordan, A.B. Harris, M. Gell, J. Roth, Double-layer gadolinium Zirconate/Yttria-Stabilized Zirconia thermal barrier coatings deposited by the solution precursor Plasma spray process, J. Therm. Spray Technol. 24 (2015) 895–906, https://doi.org/10.1007/s11666-015-0283-6.

[47] R. Kumar, D. Cietek, C. Jiang, J. Roth, M. Gell, E.H. Jordan, Influence of microstructure on the durability of gadolinium zirconate thermal barrier coatings using APS & SPPS processes, Surf. Coat. Technol. 337 (2018) 117–125, https://doi.org/10.1016/j.surfcoat.2018.01.004.

[48] S.V. Joshi, G. Sivakumar, Hybrid processing with powders and solutions: a novel approach to deposit composite coatings, J. Therm. Spray Technol. 24 (2015) 1166–1186, https://doi.org/10.1007/s11666-015-0262-y.

[49] H. Hou, J. Veilleux, F. Gitzhofer, Q. Wang, Y. liu, Hybrid suspension/solution precursor plasma spraying of a complex Ba(Mg1/3Ta2/3)O3 perovskite: effects of processing parameters and precursor chemistry on phase formation and decomposition, J. Therm. Spray Technol. 28 (2019) 12–26, https://doi.org/10.1007/s11666-018-0797-9.

[50] H. Khatibnezhad, F. Ben Ettouil, C. Moreau, Photoactive Ce-doped TiO2 and CeO2-TiO2 composite coatings deposited by suspension/solution plasma spray, Mater. Res. Bull. 166 (2023), https://doi.org/10.1016/j.materresbull.2023.112346.

[51] K. VanEvery, M.J.M. Krane, R.W. Trice, W. Porter, M. Besser, H. Wang, D. Sordelet, J. Ilavsky, J. Almer, In-Flight alloying of nanocrystalline Yttria-stabilized zirconia using suspension spray to produce ultra-low thermal conductivity thermal barriers, Int. J. Appl. Ceram. Technol. 8 (2011) 1382–1392, https://doi.org/10.1111/j.1744-7402.2010.02593.x.

[52] S. Gong, K. VanEvery, H. Wang, R.W. Trice, Microstructure and thermal properties of inflight rare-earth doped thermal barriers prepared by suspension plasma spray,

J. Eur. Ceram. Soc. 34 (2014) 1243–1253, https://doi.org/10.1016/j.jeurceramsoc.2013.11.016.
[53] X. Meng, W. Ma, T. Yang, W. Huang, E. Li, Y. Bai, C. Liu, H. Dong, Microstructure and thermal properties of double rare-earth Co-doped SrZrO3 coating by the solution precursor plasma spray, J. Therm. Spray Technol. 29 (2020) 125–133, https://doi.org/10.1007/s11666-019-00974-x.
[54] M. Sebastiani, K.E. Johanns, E.G. Herbert, F. Carassiti, G.M. Pharr, A novel pillar indentation splitting test for measuring fracture toughness of thin ceramic coatings, Philos. Mag. 95 (2015) 1928–1944, https://doi.org/10.1080/14786435.2014.913110.
[55] T. Beirau, E. Rossi, M. Sebastiani, W.C. Oliver, H. Pöllmann, R.C. Ewing, Fracture toughness of radiation-damaged zircon studied by nanoindentation pillar-splitting, Appl. Phys. Lett. 119 (2021), https://doi.org/10.1063/5.0070597.
[56] Y. Wu, H. Luo, C. Cai, Y. Wang, Y. Zhou, L. Yang, G. Zhou, Comparison of CMAS corrosion and sintering induced microstructural characteristics of APS thermal barrier coatings, J. Mater. Sci. Technol. 35 (2019) 440–447, https://doi.org/10.1016/j.jmst.2018.09.046.
[57] G. Boissonnet, F. Pedraza, C. Chalk, J.R. Nicholls, G. Bonnet, Thermal insulation of YSZ and Erbia-doped yttria-stabilised zirconia EB-PVD thermal barrier coating systems after CMAS attack, Materials 13 (2020) 1–16, https://doi.org/10.3390/ma13194382.
[58] K. VanEvery, M.J.M. Krane, R.W. Trice, H. Wang, W. Porter, M. Besser, D. Sordelet, J. Ilavsky, J. Almer, Column formation in suspension plasma-sprayed coatings and resultant thermal properties, J. Therm. Spray Technol. 20 (2011) 817–828, https://doi.org/10.1007/s11666-011-9632-2.
[59] R. Tuncer, M. Karabaş, H. Gökçe, Y. Kayalı, Effect of Yb, Fe and Mo, Ti Co-doping on thermal and mechanical properties of Gd2Zr2O7 ceramics, Ceram. Int. 51 (2025) 28678–28688, https://doi.org/10.1016/j.ceramint.2025.04.075.
[60] S. Bursich, S. Morelli, G. Bolelli, G. Cavazzini, E. Rossi, F.G. Mecca, S. Petruzzi, E. Bemporad, L. Lusvarghi, The effect of ceramic YSZ powder morphology on coating performance for industrial TBCs, Surf. Coat. Technol. 476 (2024) 130270, https://doi.org/10.1016/J.SURFCOAT.2023.130270.
[61] C. Mercer, J.R. Williams, D.R. Clarke, A.G. Evans, On a ferroelastic mechanism governing the toughness of metastable tetragonal-prime (t′) yttria-stabilized zirconia, Proc. R. Soc. A 463 (2007) 1393–1408, https://doi.org/10.1098/rspa.2007.1829.
[62] S. Tseng, C. Chao, D. Li, X. Fan, Experimental and simulation analysis of the evolution of residual stress due to expansion via CMAS infiltration in thermal barrier coatings, Coatings 11 (2021), https://doi.org/10.3390/coatings11101148.